

https://dspace.org/

Topochemical reactions of lithium with transition metal oxides

Picciotto, Lucette Andree

2015-03-04
http://hdl.handle.net/10539/17117

Downloaded from a DSpace repository. https://dspace.org/

TOPOCHEMICAL REACTIONS OF LITHIUM WITH TRANSITION METAL OXIDES

Lucette Andrée de Picciotto

A Thesis submitted to the Faculty of Science
University of the Witwatersrand, Johannesburg
in fulfilment of the requirements for the
Degree of Doctor of Philosophy

Johannesburg 1988

ABSTRACT

Topochemical reactions of lithium with various transition metal oxides are investigated with a special emphasis on spinels. Reactions are carried out both with chemical reagents and in electrochemical cells. The products are structurally characterised by powder X-ray diffraction. The determination of electrochemical curves, galvanostatic discharge curves, lithium-ion diffusion rates and cyclic voltammetry are used to study the cell reactions.

Lithium is extracted from $LiVO_2$ forming $Li_{0.2}VO_2$, where approximately one-third of the vanadium ions migrate to the octahedral 3a sites, formerly occupied solely by lithium; the remaining two-thirds reside in the octahedral 3b sites, as in $LiVO_2$. This transformation is irreversible.

When heated to 300°C, the two-phase intermediate products $Li_{0.5}VO_2$ and $Li_{0.45}VO_2$ transform to the spinel structures LiV_2O_4 and metastable $Li_{0.9}V_2O_4$. The conversion and the structure of these products are described.

Lithiation of the spinel $Li[V_2]O_4$ leads to the partially ordered rocksalt phase $Li_2[V_2]O_4$, where the spinel $[B_2]X_4$ sub-lattice remains intact. The reaction is reversible and exhibits a discharge plateau at ~2.350 V. Delithiation of LiV_2O_4 is accompanied by an irreversible rearrangement of the vanadium cations, resulting in a defect rocksalt phase, where the latter are distributed in alternate layers of octahedra of the oxide lattice with a ratio of 5 : 3 (in spinel, this ratio is 3 : 1). Relithiation is possible, but proceeds according to a different mechanism.

Lithium diffusion rates in the system $Li_{1+x}V_2O_4$ $(0 \leq x \leq 1)$ vary between 4.10^{-10} cm^2/sec $(x = 0)$ to 6.10^{-8} cm^2/sec $(x = 1)$. In

delithiated $Li_{1-x}V_2O_4$, $\tilde{D} = 1.10^{-9}$ cm^2/sec; in layered $LiVO_2$, $\tilde{D} = 5.10^{-9}$ cm^2/sec. Li^+ diffusion rates in the spinels $LiMn_2O_4$ and Fe_3O_4 are determined for comparison.

In order to stabilise delithiated $Li_{1-x}V_2O_4$ ($0.3<x<0.8$), partial substitution of Li^+ with Zn^{2+} is carried out by ion exchange. The compounds $Li_xZn_yV_2O_4$ ($0.73<x<0.84$; $0.04<y<0.10$) are formed and structurally characterised. Stabilisation of the spinel $[B_2]X_4$ framework is attained for relatively high lithium content in $Li_{1-x}V_2O_4$. Further delithiation leads to concurrent zinc extraction, which is accompanied by the irreversible vanadium-ion migration, already observed in the unsubstituted material.

The electrostatic energy and site self-potentials of the lithiated spinels $Li_xMn_3O_4$ and $Li_{1+x}Mn_2O_4$ ($0<x<1$) were calculated and partly clarify their different lithiation mechanisms.

DECLARATION

I declare that this thesis is my own, unaided work. It is being submitted for the degree of Doctor of Philosophy in the University of the Witwatersrand, Johannesburg. It has not been submitted before for any degree or examination in any other University.

Lynette de Pianto

28th day of July, 1988.

TO MY PARENTS

ACKNOWLEDGEMENTS

I would like to express my gratitude to my supervisors Prof J C A Boeyens and Dr M M Thackeray for their guidance, advice and the many useful discussions throughout this work, and for always being available for assistance and encouragement.

I would also like to thank Prof L Glasser for his constructive suggestions and criticism while Prof J C A Boeyens was on sabbatical leave.

Dr G G Garrett, Chief Director of the National Institute for Materials Research, is thanked for his permission to use the research done at this institute for this thesis.

A special word of thanks goes to my colleagues at the NIMR for the many scientific discussions, for their technical assistance and for their constant encouragement during this work.

Mr H H Lachmann is thanked for doing the atomic absorption analyses.

Mrs J Turnbull is thanked for doing part of the drawings.

Financial assistance from the Council for Scientific and Industrial Research is gratefully acknowledged.

I would also like to thank Adele Forman for her competent typing of this thesis and for her patience in deciphering my handwriting and when faced with so many alterations.

Finally, I thank my parents and my brother Raffaele for their constant encouragement and moral support, without which this thesis would not have been possible.

CONTENTS

	PAGE
ABSTRACT	ii
ACKNOWLEDGEMENTS	vi
CONTENTS	vii
LIST OF TABLES	xvii
LIST OF FIGURES	xxv
PUBLICATIONS	xxxi
CHAPTER 1: INTRODUCTION	1
1.1 INTERCALATION REACTIONS	3
1.1.1 Definition	3
1.1.2 Applications	4
1.1.3 Intercalation compounds as solid state cathode materials	4
1.1.4 Choice of lithium as an anode	6
1.1.5 Brief review of host lattices for solid state cathodes	6
1.1.5.1 Linear chain structures	7
1.1.5.2 Layered structures	8
1.1.5.3 Framework structures	10

		PAGE
1.2	SPINELS	14
	1.2.1 Definition	14
	1.2.2 General methods of preparation	14
	1.2.3 The spinel structure	15
	1.2.3.1 Introduction	15
	1.2.3.2 Interatomic distances and the u parameter	17
	1.2.3.3 Lower symmetry spinels	20
	1.2.3.3.i Superstructures	20
	1.2.3.3.ii Lattice distortion	21
	1.2.4 Cation distribution	22
	1.2.4.1 Introduction	22
	1.2.4.2 Experimental determination	22
	1.2.4.3 Theoretical models	24
1.3	STRUCTURE OF $LiMO_2$ COMPOUNDS (M=V, Co, Cr, Ni)	26
1.4	LITHIUM INSERTION/EXTRACTION REACTIONS WITH OXO-SPINELS	28
	1.4.1 General	28
	1.4.2 Interstitial sites in spinels	29
	1.4.3 The $Li[M_2]O_4$ (M=Ti, V, Mn) spinels	30
1.5	AIM OF THIS WORK	31

		PAGE
CHAPTER 2:	OVERVIEW OF EXPERIMENTAL TECHNIQUES	33
2.1	POWDER X-RAY DIFFRACTION	33
2.1.1	History of X-ray diffraction	33
2.1.2	The Bragg Law	34
2.1.3	Choice of powder X-ray diffraction	36
2.1.4	Structure determination by powder X-ray diffraction	37
2.1.4.1	Symmetry of the unit cell and lattice constants	37
2.1.4.2	Atomic positions	38
2.1.5	Instrumentation : the diffractometer	42
2.2	DIFFERENTIAL SCANNING CALORIMETRY (DSC)	45
2.2.1	Principle	45
2.2.2	Instrumentation	46
2.3	THERMODYNAMICS OF ELECTROCHEMICAL CELLS: ELECTROCHEMICAL CURVES	47
2.4	GALVANOSTATIC DISCHARGE CURVES	51
2.5	CYCLIC VOLTAMMETRY	54
2.5.1	General principles	54
2.5.2	Instrumentation	60
2.5.3	Cyclic voltammetry of intercalation systems	60

		PAGE
2.6	LITHIUM DIFFUSION RATES ($\tilde{D}$)	62
	2.6.1 General principles	62
	2.6.2 The galvanostatic pulse-relaxation technique by Basu and Worrell	64
	2.6.3 Critical evaluation	66
CHAPTER 3:	GENERAL EXPERIMENTAL PROCEDURES	68
3.1	CHEMICAL LITHIATION WITH N-BUTYLLITHIUM	68
3.2	LITHIUM EXTRACTION BY CHEMICAL METHODS	69
	3.2.1 Lithium extraction by bromine oxidation	69
	3.2.2 Lithium extraction by acid treatment	69
	3.2.3 Lithium concentrations	70
3.3	ELECTROCHEMICAL STUDIES	70
	3.3.1 Electrochemical- and discharge-curve cells	70
	3.3.2 Cyclic voltammetry cells	73
	3.3.3 Determination of lithium diffusion rates	74
3.4	POWDER X-RAY DIFFRACTION WORK	75
3.5	DIFFERENTIAL SCANNING CALORIMETRY (DSC)	75

	PAGE
CHAPTER 4: LITHIUM EXTRACTION FROM $LiVO_2$	76
4.1 INTRODUCTION	76
4.2 EXPERIMENTAL	77
4.3 RESULTS	78
4.4 STRUCTURE OF $Li_{0.22}VO_2$	80
4.4.1 Structure determination	80
4.4.2 Discussion	92
4.5 ELECTROCHEMICAL CHARACTERISATION	96
4.5.1 Electrochemical curve	96
4.5.2 Cyclic voltammetry of $LiVO_2$	99
4.5.3 Li^+ diffusion rate in $LiVO_2$	103
4.6 CONCLUSIONS	103
CHAPTER 5: THE TRANSFORMATION OF DELITHIATED $LiVO_2$ INTO THE SPINEL STRUCTURE	107
5.1 INTRODUCTION	107
5.2 EXPERIMENTAL	108
5.3 RESULTS	108

		PAGE
5.4	STRUCTURE OF $Li_{0.9}V_2O_4$ AND $Li_{1.0}V_2O_4$	112
	5.4.1 Structural characterisation	112
	5.4.2 Discussion	117
5.5	DSC STUDY OF THE CONVERSION OF $Li_{\sim 0.45}VO_2$ TO $Li_{\sim 0.90}V_2O_4$	123
5.6	CONCLUSIONS	126
CHAPTER 6:	LITHIUM INSERTION INTO LiV_2O_4	128
6.1	INTRODUCTION	128
6.2	EXPERIMENTAL	128
6.3	RESULTS	129
6.4	STRUCTURAL CHARACTERISATION OF $Li_{1.5}V_2O_4$ AND $Li_{2.0}V_2O_4$	130
	6.4.1 Structure determination of $Li_{1.5}V_2O_4$	136
	6.4.2 Structure determination of $Li_{2.0}V_2O_4$	140
6.5	ELECTROCHEMICAL CHARACTERISATION	144
	6.5.1 Electrochemical curve	144
	6.5.2 Constant current discharge curve	146

	PAGE
6.5.3 Cyclic voltammetry of the system $Li_{1+x}V_2O_4$	146
6.5.4 Li^+ diffusion rate in the system $Li_{1+x}V_2O_4$ ($0<x<1$)	151
6.6 REACTION MECHANISM	157
6.7 CONCLUSIONS	160
CHAPTER 7: LITHIUM EXTRACTION FROM LiV_2O_4	165
7.1 INTRODUCTION	165
7.2 EXPERIMENTAL	165
7.3 RESULTS	166
7.4 INTERPRETATION OF THE STRUCTURAL DATA	173
7.4.1 $Li_{1-x}V_2O_4$, where $0<x<0.34$	173
7.4.2 $Li_{1-x}V_2O_4$, where $0.34<x<0.73$	173
7.4.3 Structure of $Li_{0.28}V_2O_4$	175
7.5 ELECTROCHEMICAL CHARACTERISATION	177
7.5.1 Electrochemical curve	177
7.5.2 Cyclic voltammetry of the system $Li_{1\pm x}V_2O_4$	179
7.5.3 Lithium diffusion rate in $Li_{0.28}V_2O_4$	187

	PAGE
7.6 DISCUSSION	187
7.7 CONCLUSIONS	189
CHAPTER 8: FORMATION AND DELITHIATION OF $Li_xZn_yV_2O_4$ ($0.73<x<0.84$; $0.04<y<0.10$)	191
8.1 INTRODUCTION	191
8.1.1 Choice of zinc as a dopant	191
8.1.2 Literature survey of solid solutions with LiV_2O_4	192
8.1.3 Spinel preparation by ion exchange	193
8.2 EXPERIMENTAL	195
8.3 FORMATION OF $Li_xZn_yV_2O_4$ ($0.73<x<0.84$; $0.04<y<0.10$)	196
8.4 STRUCTURE OF $Li_xZn_yV_2O_4$ ($x\approx0.80$, $y\approx0.05$)	199
8.5 LITHIUM EXTRACTION FROM $Li_xZn_yV_2O_4$ ($0.73<x<0.84$; $0.04<y<0.10$)	206
8.5.1 Results	206
8.5.2 Structure	207
8.6 CYCLIC VOLTAMMETRY OF $Li_{0.77}Zn_{0.08}V_2O_4$	212
8.7 DISCUSSION AND CONCLUSIONS	216

PAGE

CHAPTER 9: ELECTROSTATIC ENERGY OF THE LITHIATED SPINELS $Li_xMn_3O_4$ AND $Li_{1+x}Mn_2O_4$ $(0<x\leq1)$ 218

9.1 INTRODUCTION 218

9.2 LATTICE ENERGY IN IONIC CRYSTALS 219

9.3 ELECTROSTATIC ENERGY AND THE MADELUNG CONSTANT 222

9.4 SHORT SURVEY OF METHODS FOR EVALUATING THE MADELUNG ENERGY 224

9.5 CALCULATION OF MADELUNG ENERGIES BY THE PLANEWISE SUMMATION METHOD (PSM) 226

9.6 LATTICE ENERGY OF SPINELS: A BRIEF SURVEY OF THE LITERATURE 228

9.7 MECHANISM OF LITHIUM INSERTION INTO Mn_3O_4 AND $LiMn_2O_4$ 230

9.8 PROGRAM USED FOR CALCULATION 232

9.9 DATA FOR THE EVALUATION OF THE ELECTROSTATIC ENERGIES OF $Li_xMn_3O_4$ AND $Li_{1+x}Mn_2O_4$ $(0<x\leq1)$ 234

9.10 RESULTS AND DISCUSSION 236

9.11 CONCLUSIONS 263

PAGE

CHAPTER 10: GENERAL CONCLUSIONS AND SUGGESTIONS FOR FURTHER WORK 265

APPENDIX: CONTRIBUTION OF VARIOUS ATOM POSITIONS TO THE INTENSITIES OF SELECTED REFLECTIONS IN THE $Fd\bar{3}m$ AND $R\bar{3}m$ SPACE GROUPS 270

REFERENCES 276

LIST OF TABLES

		PAGE
CHAPTER 1		
Table 1.1	Interatomic distances in spinels as a function of "a" and "u"	18
CHAPTER 4		
Table 4.1	Lattice parameters and method of preparation of various samples of $Li_{1-x}VO_2$	79
Table 4.2	Powder X-ray diffraction pattern of $Li_{0.2}VO_2$	86
Table 4.3a	Structural parameters of $Li_{0.2}VO_2$ (Model 1)	87
Table 4.3b	Observed and calculated intensities for $Li_{0.2}VO_2$ (Model 1)	87
Table 4.4a	Structural parameters of $Li_{0.2}VO_2$ (Model 2)	89
Table 4.4b	Observed and calculated intensities for $Li_{0.2}VO_2$ (Model 2)	89
Table 4.5	Structural parameters of $Li_{0.2}VO_2$ (Model 3)	91
Table 4.6	Structural parameters of $Li_{0.2}VO_2$ (Model 4)	91

		PAGE
CHAPTER 5		
Table 5.1	X-ray diffraction pattern of $Li_{0.9}V_2O_4$	110
Table 5.2	X-ray diffraction pattern of $Li_{1.0}V_2O_4$	111
Table 5.3a	Structural parameters of $Li_{0.9}V_2O_4$ (Model 1)	113
Table 5.3b	Observed and calculated intensities for $Li_{0.9}V_2O_4$ (Model 1)	113
Table 5.4a	Structural parameters of $Li[V_2]O_4$ (Model 1)	113
Table 5.4b	Observed and calculated intensities for $Li[V_2]O_4$ (Model 1)	114
Table 5.5a	Structural parameters of $Li_{0.9}V_2O_4$ (Model 2)	116
Table 5.5b	Observed and calculated intensities for $Li_{0.9}V_2O_4$ (Model 2)	116
Table 5.6a	Structural parameters of $Li_{1.0}V_2O_4$ (Model 2)	116
Table 5.6b	Observed and calculated intensities for $Li_{1.0}V_2O_4$ (Model 2)	117

CHAPTER 6

		PAGE
Table 6.1	Cell constants of various phases $Li_{1+x}V_2O_4$	130
Table 6.2	Powder X-ray diffraction pattern of $Li_{1.5}V_2O_4$	134
Table 6.3	Powder X-ray diffraction pattern of $Li_{2.0}V_2O_4$	135
Table 6.4a	Structural parameters of $Li_{1.5}V_2O_4$ (Model 1)	137
Table 6.4b	Observed and calculated intensities for $Li_{1.5}V_2O_4$ (Model 2)	137
Table 6.5a	Structural parameters of $Li_{1.5}V_2O_4$ (Model 2)	139
Table 6.5b	Observed and calculated intensities for $Li_{1.5}V_2O_4$ (Model 2)	139
Table 6.6a	Structural parameters of $Li_{1.5}V_2O_4$ (Model 3)	141
Table 6.6b	Observed and calculated intensities for $Li_{1.5}V_2O_4$ (Model 3)	141
Table 6.7a	Structural parameters of $Li_{2.0}V_2O_4$	143
Table 6.7b	Observed and calculated intensities for $Li_{2.0}V_2O_4$	143
Table 6.8	Cathodic and anodic peak potentials (E_{pc}, E_{pa}), ΔE_p and mean potential $\bar{E}$ for different scan rates	149
Table 6.9	Lithium diffusion rates in $Li_{1+x}V_2O_4$, $LiVO_2$, $LiMn_2O_4$ and Fe_3O_4	153

		PAGE
CHAPTER 7		
Table 7.1	Structural data for a few samples of $Li_{1-x}V_2O_4$	167
Table 7.2	Relative intensities of LiV_2O_4, $Li_{0.27}V_2O_4$ and $Li_{0.2}VO_2$	174
Table 7.3a	Structural parameters of $Li_{0.28}V_2O_4$	176
Table 7.3b	X-ray diffraction pattern of $Li_{0.28}V_2O_4$ with calculated and observed intensities	177
CHAPTER 8		
Table 8.1	Composition, temperature of preparation and cell constants of a few $Li_xZn_yV_2O_4$ samples	196
Table 8.2	Powder X-ray diffraction pattern of $Li_{0.84}Zn_{0.05}V_2O_4$	200
Table 8.3	Powder X-ray diffraction pattern of $Li_{0.77}Zn_{0.04}V_2O_4$	201
Table 8.4	Structural parameters of $Li_{0.84}Zn_{0.05}V_2O_4$ (Model 1)	203

		PAGE
Table 8.5	Structural parameters of $Li_{0.77}Zn_{0.04}V_2O_4$ (Model 1)	203
Table 8.6	Structural parameters of $Li_{0.84}Zn_{0.05}V_2O_4$ (Model 2)	204
Table 8.7	Structural parameters of $Li_{0.77}Zn_{0.04}V_2O_4$ (Model 2)	204
Table 8.8	Structural parameters of $Li_{0.84}Zn_{0.05}V_2O_4$ (Model 3)	205
Table 8.9	Structural parameters of $Li_{0.77}Zn_{0.04}V_2O_4$ (Model 3)	205
Table 8.10	Results of lithium extraction from $Li_xZn_yV_2O_4$	207
Table 8.11	Peak intensities for a few $Li_xZn_yV_2O_4$ compounds	211
CHAPTER 9		
Table 9.1	Contributions of various components of the lattice energy in alkali halides	221
Table 9.2	Structural data of reactants and lithiated products	235
Table 9.3	Corresponding sites in Fd3m and $I4_1/amd$	235

		PAGE
Table 9.4a	Charges and self-potentials of $Li_xMn_3O_4$ ($0<x<1$) according to model 1	242
Table 9.4b	Total electrostatic energy of $Li_xMn_3O_4$ ($0<x<1$) and contributions from each site (Model 1)	243
Table 9.5a	Charges and self-potentials of $Li_xMn_3O_4$ ($0<x<1$) according to model 2	243
Table 9.5b	Total electrostatic energy of $Li_xMn_3O_4$ ($0<x<1$) and contributions from each site (Model 2)	244
Table 9.6a	Charges and self-potentials of $Li_{1+x}Mn_2O_4$ ($0<x<1$) according to model 1	244
Table 9.6b	Total electrostatic energy of $Li_{1+x}Mn_2O_4$ ($0<x<1$) and contributions from each site (Model 1)	245
Table 9.7a	Charges and self-potentials of $Li_{1+x}Mn_2O_4$ ($0<x<1$) according to model 2	245
Table 9.7b	Total electrostatic energy of $Li_{1+x}Mn_2O_4$ ($0<x<1$) and contributions from each site (Model 2)	246
Table 9.8a	Charges and self-potentials of $Li_2Mn_2O_4$ (random distribution of lithium in the 8a and 16c sites)	246

		PAGE
CHAPTER 9 (CONTINUED)		
Table 9.8b	Electrostatic energy of $Li_2Mn_2O_4$ and contributions from each site (random distribution)	246
Table 9.9	Cation-cation interactions in $Li_xMn_3O_4$ ($0<x<1$) (Model 1) a) Charges and self-potentials b) Energy (E_{cc}) due to the cation-cation interactions, and contributions of each site	247
Table 9.10	Cation-cation interactions in $Li_xMn_3O_4$ ($0<x<1$) (Model 2) a) Charges and self-potentials b) Energy (E_{cc}) due to the cation-cation interactions, and contributions of each site	248
Table 9.11	Cation-cation interactions in $Li_{1+x}Mn_2O_4$ ($0<x<1$) (Model 1) a) Charges and self-potentials b) Energy (E_{cc}) due to the cation-cation interactions, and contributions of each site	249
Table 9.12	Cation-cation interactions in $Li_{1+x}Mn_2O_4$ ($0<x<1$) (Model 2) a) Charges and self-potentials b) Energy (E_{cc}) due to the cation-cation interactions, and contributions of each site	250

PAGE

CHAPTER 9 (CONTINUED)

Table 9.13 Cation-cation interactions in $Li_2Mn_2O_4$ with a random distribution of lithium in the 8a and 16c sites 251
a) Charges and self-potentials
b) Energy (E_{cc}) due to the cation-cation interactions, and contributions of each site

APPENDIX

Table A.1 Atom positions for the space-group Fd3m 272

Table A.2 Values of a, b in the space-group Fd3m for a few reflections 272

Table A.3 Atom positions for the space-group $R\bar{3}m$ 273

Table A.4 Values of a, b in the space-group $R\bar{3}m$ for a few reflections 274

LIST OF FIGURES

PAGE

CHAPTER 1

Fig 1.1	Basic categories of host lattices	7
Fig 1.2	Structure of $NbSe_3$	8
Fig 1.3	Structure of TiS_2	9
Fig 1.4	Cuboctahedral cavities in ReO_3 and WO_3	11
Fig 1.5	Shearing of ReO_3 structure resulting in V_2O_5 and V_6O_{13}	12
Fig 1.6	Structure of LiV_2O_5	12
Fig 1.7	Channels in the rutile structure	13
Fig 1.8	Unit cell of the spinel structure	15
Fig 1.9	Atomic and interstitial sites in the spinel structure	16
Fig 1.10	Nearest neighbours of the anion (X) in the spinel structure	19
Fig 1.11	Structure of $LiMO_2$ (M=V,Co,Cr,Ni)	27

CHAPTER 2

Fig 2.1	Diffraction by planes of atoms in a crystal	35
Fig 2.2	The diffractometer assembly	43
Fig 2.3	The focusing circle	44
Fig 2.4	The DSC heating system	47
Fig 2.5	Typical galvanostatic discharge curve	53
Fig 2.6	Applied potential waveform in cyclic voltammetry	55
Fig 2.7	Cyclic voltammogram of a single reversible process	55

PAGE

CHAPTER 3

Fig 3.1 The ambient temperature electrochemical cell 71

Fig 3.2 The ambient temperature cyclic voltammetry cell 73

CHAPTER 4

Fig 4.1 X-ray diffraction pattern of $LiVO_2$ 81

Fig 4.2 X-ray diffraction pattern of $Li_{0.5}VO_2$ 82

Fig 4.3 X-ray diffraction pattern of $Li_{0.2}VO_2$ 83

Fig 4.4 Ambient temperature electrochemical curve of the cell $LiVO_2 \mid LiClO_4$ 1M (P.C.) $\mid LiMn_2O_4$ 97

Fig 4.5 Cyclic voltammogram of $LiVO_2$ 100

Fig 4.6 Cyclic voltammogram of the system $Li_{1-x}VO_2$ $(0<x<1)$ 102

CHAPTER 5

Fig 5.1 X-ray diffraction pattern of $Li_{0.9}V_2O_4$ 118

Fig 5.2 X-ray diffraction pattern of $Li_{1.0}V_2O_4$ 119

Fig 5.3 X-ray diffraction pattern of LiV_2O_4 (high temperature synthesis) 120

Fig 5.4 DSC profile of the transformation $Li_{\sim 0.45}VO_2 \longrightarrow Li_{\sim 0.9}V_2O_4$ 125

PAGE

CHAPTER 6

Fig 6.1	Variation of the cell constant ("a") as a function of the cumposition $Li_{1+x}V_2O_4$	131
Fig 6.2	X-ray diffraction pattern of $Li_{1.5}V_2O_4$	132
Fig 6.3	X-ray diffraction pattern of $Li_{2.0}V_2O_4$	132
Fig 6.4	Ambient temperature electrochemical curve of the cell $Li/LiClO_4$ 1M (P.C.)/$Li_{0.94}V_2O_4$	145
Fig 6.5	Constant current discharge curve of the cell $Li/LiClO_4$, 1M (P.C.)/$Li_{0.98}V_2O_4$ at 25 °C (20 μA, 10 mg LiV_2O_4)	147
Fig 6.6	Cyclic voltammogram of the system $Li_{1+x}V_2O_4$ ($0<x<1$) (v = 1 mV/sec)	148
Fig 6.7	Cyclic voltammogram of the system $Li_{1+x}V_2O_4$ ($0<x<1$) (v = 0.5 mV/sec)	150
Fig 6.8	Variation of $\tilde{D}$ as a function of lithium content in $Li_{1+x}V_2O_4$ ($0<x<1$)	152
Fig 6.9	Schematic representation of the site energy differences between the 8a and 16c sites in spinel and rocksalt	155
Fig 6.10	Constant current discharge curves of the cells $Li/LiClO_4$ 1M (P.C.)/$Li[M_2]O_4$ (M=Ti,V,Mn) (20 $\mu A/cm^2$)	162
Fig 6.11	Cyclic voltammogram of $LiMn_2O_4$ (v = 1 mV/sec)	163

PAGE

CHAPTER 7

Fig 7.1	Variation of the lattice parameter "a" with composition, x, in $Li_{1-x}V_2O_4$	168
Fig 7.2	X-ray diffraction pattern of $Li_{0.72}V_2O_4$	169
Fig 7.3	X-ray diffraction pattern of $Li_{0.45}V_2O_4$	170
Fig 7.4	X-ray diffraction pattern of $Li_{0.27}V_2O_4$ (two-phase)	171
Fig 7.5	X-ray diffraction pattern of $Li_{0.28}V_2O_4$ (cubic)	172
Fig 7.6	Ambient temperature electrochemical curve of the cell $Li_{\sim 0.95}V_2O_4/LiClO_4$ 1M (P.C.)/$LiMn_2O_4$	178
Fig 7.7	Cyclic voltammogram of the system $Li_{1\pm x}V_2O_4$ (initial scan : anodic; v = 0.5 mV/sec)	181
Fig 7.8	Cyclic voltammogram of the system $Li_{1\pm x}V_2O_4$ (initial scan : anodic; v = 1.0 mV/sec)	182
Fig 7.9	Cyclic voltammogrsm of the system $Li_{1\pm x}V_2O_4$ (initial scan : cathodic; v = 1.0 mV/sec)	183
Fig 7.10	Cyclic voltammogram of the system $Li_{1\pm x}V_2O_4$ (initial scan : cathodic; v = 0.5 mV/sec)	184
Fig 7.11	Cyclic voltammogram of the system $Li_{1\pm x}V_2O_4$ (initial scan : cathodic; v = 0.1 mV/sec)	185

CHAPTER 8

Fig 8.1	X-ray diffraction pattern of $Li_{0.84}Zn_{0.05}V_2O_4$	197
Fig 8.2	X-ray diffraction pattern of $Li_{0.79}Zn_{0.10}V_2O_4$	198
Fig 8.3	X-ray diffraction pattern of $Li_{0.65}Zn_{0.04}V_2O_4$	208
Fig 8.4	X-ray diffraction pattern of $Li_{0.53}Zn_{0.02}V_2O_4$	209
Fig 8.5	X-ray diffraction pattern of $Li_{0.34}Zn_{0.01}V_2O_4$	210

PAGE

CHAPTER 8 (CONTINUED)

Fig 8.6 Cyclic voltammogram of the system $Li_{0.77+x}Zn_{0.08}V_2O_4$ (initial scan : cathodic; v = 1 mV/sec) 213

Fig 8.7 Cyclic voltammogram of the system $Li_{0.77\pm x}Zn_{0.08}V_2O_4$ (initial scan : anodic; v = 1 mV/sec) 214

Fig 8.8 Cyclic voltammogram of the system $Li_{0.77\pm x}Zn_{0.08}V_2O_4$ (initial scan : cathodic; v = 1 mV/sec) 215

CHAPTER 9

Fig 9.1 Electrostatic energy of $Li_xMn_3O_4$ ($0<x<1$) according to models 1 and 2 252

Fig 9.2 Electrostatic energy of $Li_{1+x}Mn_2O_4$ ($0<x<1$) according to models 1, 2 and with a random distribution on the 8a and 16c sites 253

Fig 9.3 Self-potential of the 32e sites in $Li_xMn_3O_4$ ($0<x<1$) according to models 1 and 2 254

Fig 9.4 Self-potential of the 16d sites in $Li_xMn_3O_4$ ($0<x<1$) according to models 1 and 2 255

Fig 9.5 Self-potential of the 32e sites in $Li_{1+x}Mn_2O_4$ ($0<x<1$) according to models 1 and 2 with a random distribution on the 8a and 16c sites 256

Fig 9.6 Self-potential of the 16d sites in $Li_{1+x}Mn_2O_4$ ($0<x<1$) according to models 1 and 2 and with a random distribution on the 8a and 16c sites 257

PAGE

CHAPTER 9 (CONTINUED)

Fig 9.7	Self-potentials of the 8a and 16c sites in $Li_xMn_3O_4$ ($0<x<1$) according to models 1 and 2	258
Fig 9.8	Self-potentials of the 8a and 16c sites in $Li_{1+x}Mn_2O_4$ ($0<x<1$) according to models 1 and 2 and with a random distribution on the 8a and 16c sites	259
Fig 9.9	Electrostatic energy of the 8a and 16c sites in $Li_xMn_3O_4$ ($0<x<1$) according to models 1 and 2	260
Fig 9.10	Electrostatic energy of the 8a and 16c sites in $Li_{1+x}Mn_2O_4$ ($0<x<1$) according to models 1 and 2 and with a random distribution on the 8a and 16c sites	261
Fig 9.11	Cation-cation interactions in $Li_xMn_3O_4$ and $Li_{1+x}Mn_2O_4$ ($0<x<1$) according to various models	262

PUBLICATIONS

Sections of this work have been published.

1. Structural characterization of delithiated $LiVO_2$.
   L A de Picciotto, M M Thackeray, W I F David, P G Bruce and J B Goodenough.
   Mater. Res. Bull. **19** , 1497 (1984)

2. Transformation of delithiated $LiVO_2$ to the spinel structure.
   L A de Picciotto and M M Thackeray.
   Mater. Res. Bull., **20** , 187 (1985)

3. Insertion/extraction reactions of lithium with LiV_2O_4.
   L A de Picciotto and M M Thackeray.
   Mater. Res. Bull., **20** , 1409 (1985)

4. Lithium insertion/extraction reactions with $LiVO_2$ and LiV_2O_4.
   L A de Picciotto and M M Thackeray.
   Solid State Ionics, **18-19,** 773 (1986). Proceedings of the 5th International Conference on Solid State Ionics, Lake Tahoe, California, USA, August 1985, Part II.

5. Lithium extraction from $Li_{1-2x}Zn_xV_2O_4$ ($0<x<0.10$).
   L A de Picciotto and M M Thackeray.
   Extended Abstracts of the III European Conference on Solid State Chemistry, Regensburg, W. Germany (May 1986).

6. Spinel electrodes for lithium batteries - a review.
   M M Thackeray, L A de Picciotto, A de Kock, P J Johnson, V A Nicholas and K T Adendorff.
   J. Power Sources, **21,** 1 (1987).

PUBLICATIONS (CONTINUED)

7. Powder X-ray diffraction pattern of lithium vanadium oxide (LiV_2O_4).
   L A de Picciotto.
   JCPDS Powder Diffraction File. In press.

8. An electrochemical study of the systems $Li_{1\pm x}V_2O_4$ and $Li_{1-x}VO_2$ ($0<x<1$).
   L A de Picciotto, M M Thackeray and G Pistoia.
   Extended Abstracts, 6th Int. Conf. Solid State Ionics, Garmisch-Partenkirchen, West Germany, September 1987.

9. Lithium insertion into $Li_{\sim 0.25}V_2O_4$.
   L A de Picciotto and M M Thackeray.
   Extended Abstracts, 6th Int. Conf. Solid State Ionics, Garmisch-Partenkirchen, West Germany, September 1987.

10. An electrochemical study of the systems $Li_{1\pm x}V_2O_4$ and $Li_{1-x}VO_2$ ($0<x<1$).
    L A de Picciotto, M M Thackeray and G Pistoia.
    Solid State Ionics (1988). In press.

PUBLICATIONS (CONTINUED)

7. Powder X-ray diffraction pattern of lithium vanadium oxide (LiV_2O_4).
   L A de Picciotto.
   JCPDS Powder Diffraction File. In press.

8. An electrochemical study of the systems $Li_{1\pm x}V_2O_4$ and $Li_{1-x}VO_2$ ($0<x<1$).
   L A de Picciotto, M M Thackeray and G Pistoia.
   Extended Abstracts, 6th Int. Conf. Solid State Ionics, Garmisch-Partenkirchen, West Germany, September 1987.

9. Lithium insertion into $Li_{\sim 0.25}V_2O_4$.
   L A de Picciotto and M M Thackeray.
   Extended Abstracts, 6th Int. Conf. Solid State Ionics, Garmisch-Partenkirchen, West Germany, September 1987.

10. An electrochemical study of the systems $Li_{1\pm x}V_2O_4$ and $Li_{1-x}VO_2$ ($0<x<1$).
    L A de Picciotto, M M Thackeray and G Pistoia.
    Solid State Ionics (1988). In press.

CHAPTER 1

INTRODUCTION

The energy crisis of the early 1970's caused a renewed interest in the development of alternative energy sources and conservation systems. This resulted in research directed towards more efficient electrical systems, amongst which were new types of primary and secondary batteries. One of the most important requirements for these batteries is a high energy density (Watt-hours/kg or Watt-hours/cm^3).

Amongst the systems that have been investigated, ambient temperature lithium batteries have proven to be promising, particularly for low-drain applications such as cardiac pacemakers, electrochromic displays, wrist watches, calculators and other devices that use currents in the $\mu A/cm^2$ range.

Other types of lithium batteries, as well as other systems, which will not be discussed here, are being developed for applications which need a high power performance, for example the electric vehicle, which requires currents in the mA/cm^2 or even the A/cm^2 range for good acceleration.

There are over a dozen primary lithium batteries already available commercially [1-3], of which a few examples are the couples Li/CuO, Li/I_2, Li/SO_2 and Li/MnO_2. More recently, a secondary lithium cell, based on the couple Li/MoS_2, has become available on the market. One of the main advantages of lithium cells is their very limited self-discharge, which allows long-term storage without a significant voltage drop.

It is known that many of these systems operate via an intercalation reaction mechanism, whereby th[illegible]ium is inserted topotactically into the structure of the cat[illegible]de during discharge.

Many more compounds are being studied today: several transition metal sulphides and oxides, such as TiS_2, WO_3, V_2O_5 and V_6O_{13} are amongst those that have received the most attention over the past decade. In many of these cases lithium has been reversibly inserted into and extracted from the host structure.

It has recently been found that spinel oxides and sulphides are capable of reversibly accommodating lithium in the interstitial sites of the lattice; the topochemical reactions of lithium with spinel compounds will be examined in detail in the course of this work.

The rever[illegible]ity of topotactic reactions has prompted studies on the use of reactants in a "discharged" state, i.e., stable compounds containing lithium.

Materials of this type include the layered oxides $LiMO_2$, where M=V,Co,Ni,Cr. It has been shown that lithium can be extracted from the compound $LiCoO_2$, without altering the structure of the lattice.

In this work lithium extraction from the isostructural compound $LiVO_2$ will be studied, with a view to converting the intermediate compound $Li_{0.5}VO_2$ to the spinel LiV_2O_4.

This chapter comprises an introduction to intercalation reactions and to the structure of spinels and of the layered compounds $LiMO_2$ (M=V,Co,Cr,Ni).

1.1 INTERCALATION REACTIONS

1.1.1 Definition

Intercalation is a solid state reaction in which a host lattice Z accepts a guest ion, atom or molecule A.

An ideal intercalation reaction involves little or no modification of the host structure, e.g., a slight expansion or contraction of the lattice.

In cases which involve more important changes of the host matrix, i.e., cleavage of certain bonds or atomic rearrangement, the process is more correctly termed a topotactic or topochemical reaction, although the term intercalation is frequently used. In this work, the terms "intercalation" and "topochemical reaction" will be considered interchangeable, as this is accepted common practice in the recent literature. Intercalation reactions typically take place at intermediate temperatures (200 - 600K); at higher temperatures the structures become unstable, and at lower temperatures the activation energy barrier for diffusion of the guest species inside the host prevents the reaction [4].

Two different types of intercalation reactions can be defined [5]. In the first case, which is of little interest to this work, the host structure is an insulator, and its effective charge remains unchanged by the reaction, as happens with sheet silicates [6]. The second type of reaction involves an electronically conducting host matrix, where the charge is altered during the reaction. In this case, there is a simultaneous uptake of ions and electrons by the host lattice, the electrons being provided by a concurrent chemical or electrochemical reaction.

The process is then termed a topotactic redox reaction, and can be described by the equation:

$$x A^{+} + x e^{-} + Z \longrightarrow (A^{+})_{x} Z^{x-}$$

The equivalent reaction with anions, where the host lattice loses an electron, is known, although it is unusual for steric and energetic reasons and will not be discussed here.

It is immediately apparent that intercalation reactions will be readily reversible, because they do not involve extensive bond cleavage, formation of new bonds and atom reorganisation, but only minor structural changes.

1.1.2 Applications

Intercalation reactions, particularly at ambient temperature, can be used to prepare interesting substances, including non-stoichiometric compounds, with unusual valence states and/or ionic ordering. Such compounds are often metastable and unobtainable by other, more conventional methods, such as high temperature synthesis.

Many heterogeneous catalytic processes are known to take place via intercalation reactions, amongst which are included the dissolution of hydrogen in Pt, Pd and Ni, and bromine complexation by graphite.

More recently, intercalation compounds, e.g., metal oxide hydrogen bronzes, have found an application in electrochromic display devices [7,8].

In connection with the current interest in the development of more efficient systems for energy conversion and storage, many topotactic redox processes have been extensively studied as possible solid state electrode reactions for high energy density primary and secondary batteries.

1.1.3 Intercalation compounds as solid state cathode materials

Over the past 10 - 15 years, several transition metal sulphides, selenides and oxides have been investigated as solid state cathode materials for both ambient and high temperature rechargeable batteries.

The electrode reactions of these batteries may be written in the general form:

$$xA \longrightarrow xA^{+} + xe^{-}$$

$$MY_n + xe^{-} \longrightarrow M^{x-}Y_n$$

The cell reaction is thus:

$$xA + MY_n \underset{\text{charge}}{\overset{\text{discharge}}{\rightleftharpoons}} A_xMY_n$$

where A = alkali metal
M = transition metal(s)
Y = anion

The following requirements have been formulated for intercalation cathodes [9,10]:

a) A large Gibbs function ΔG, affording a high cell voltage.
b) A wide range of x in A_xMY_n, resulting in high cell capacities.
c) A limited change of ΔG over the compositional range, resulting in discharge of almost constant voltage.
d) High diffusivity of the guest ion in the host lattice.
e) Minimal modifications in the host structure (making the reaction reversible).
f) Good electronic conductivity (although a low conductivity may be enhanced by additives in the electrode).
g) Low solubility in the electrolyte.

A brief review of potential intercalation cathodes will be given in section 1.1.5.

1.1.4 Choice of lithium as an anode

Both sodium and lithium are attractive candidates as anode material, because of their high electrochemical activity and low mass. Both elements have been used as the guest ion in intercalation reactions; although sodium may be inserted into several compounds [11], lithium is generally the preferred anode for primary cells, particularly when used in conjunction with close-packed transition metal oxides and sulphides. The reasons for this preference for lithium are:

a) lithium, being a smaller atom, may be inserted more easily through atomically narrow channels.

b) lithium is the lightest alkali metal and therefore offers a superior specific anode capacity for the battery.

c) lithium is the most electropositive metal in the electrochemical series, with a standard reduction potential of -3.405V (as opposed to Na : -2.711V).

d) Sodium is commonly found in trigonal prismatic coordination, whereas lithium enjoys both tetrahedral and octahedral coordination provided by close-packed anionic arrays.

1.1.5 Brief review of host lattices for solid state cathodes

Because the feasibility of intercalation reactions is largely determined by the structure of the host, it is convenient to define three categories of host lattices (Fig 1.1):

a) one-dimensional structures, characterised by chain-type compounds.

b) two-dimensional layered compounds.

c) three-dimensional framework structures, with interconnecting channels of unoccupied lattice sites.

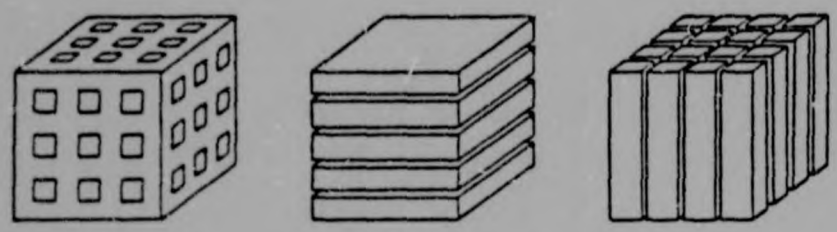


FIG 1.1
Basic categories of host lattices [4]

1.1.5.1 Linear chain structures

Very few chain-type structures have been investigated as intercalation cathode materials partly because of their low structural stability, the susceptibility of these structures to lattice defects, and the commonly encountered irreversible modifications of the host matrix caused by chemical attack [4,5]. However, a few intercalation reactions have been studied within this class of compounds, where the guest ion is inserted in the space between the chain elements.

The structure of the chalcogenide $NbSe_3$, which consists of parallel linear chains of ($NbSe_3$) (Fig 1.2), accepts up to three Li per formula unit, forming Li_3NbSe_3 [12]; the reaction is reversible.

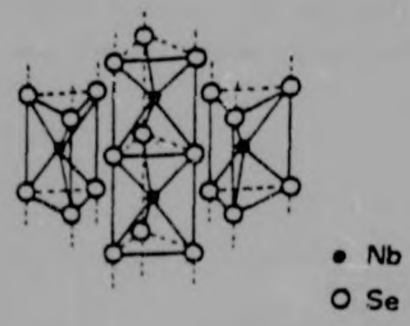


FIG 1.2
Structure of $NbSe_3$ (taken from [5])

Similarly, Na has been inserted into NbS_2Cl_2, resulting in the formation of $Na_2NbS_2Cl_2$ [11].

1.1.5.2 Layered structures

Layered compounds are probably the most extensively studied intercalation compounds; they have even been defined as the only structure that undergoes a true intercalation reaction [13].

Alkali metal intercalation compounds were prepared for the first time in 1959 [14], by reacting MoS_2 and WS_2 with a solution of the alkali metal (Li, Na, K, Rb, Cs) in ammonia at -40°C to -50 °C. Ammonia has also been intercalated into these compounds and can be removed by vacuum treatment on heating.

Research towards new forms of electrical energy storage led Whittingham [15] to propose the layered compound TiS_2 as a cathode in a high energy density lithium battery. The structure of TiS_2 (Fig 1.3) can be described as a stacking of layers of TiS_2 blocks bonded by weak van der Waals forces. The sulphide ions are hexagonally close-packed, and the Ti^{4+} ions occupy octahedral interstices.

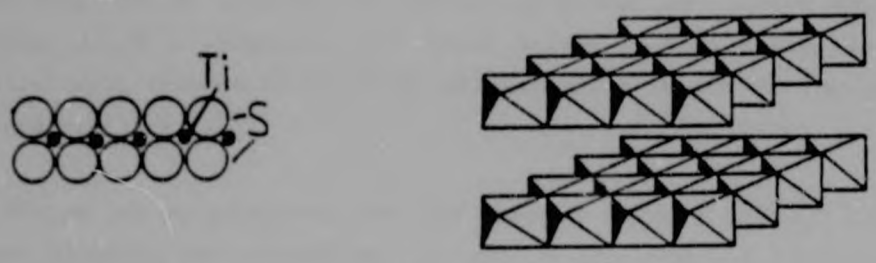


FIG 1.3
Structure of TiS_2

During the intercalation reaction, lithium is inserted into the octahedral sites located between the sulphur layers. This interstitial space between the TiS_2 blocks is often termed the van der Waals gap.

Although TiS_2 has excellent characteristics for secondary lithium cells [10,13], it suffers from a number of drawbacks common to most chalcogenides [16]:

a) sensitivity to moisture

b) relatively low energy density compared to oxides, due to the higher mass of sulphur

c) single phase intercalation reaction throughout the compositional range, which entails a sloping discharge curve

d) solvent intercalation into the structure.

These difficulties have prompted new studies of transition metal oxides as intercalation electrodes.

Amongst the layered oxides that have been studied, MoO_3 and $Mo_{18}O_{52}$ are of interest as cathode materials for lithium batteries [17,18]. However, both these oxides undergo fairly large structural changes of the host lattice, which impair the reaction reversibility [19].

Lithium can be extracted from the layered compound $LiCoO_2$, without altering the structure; at x=1 in $Li_{1-x}CoO_2$, a $CdCl_2$-type structure would be obtained [20]. The structure of the layered compounds $LiMO_2$ is described in section 1.3. The deintercalation of lithium from one of these compounds will be discussed elsewhere in this work.

1.1.5.3 Framework structures

Recent interest in transition metal oxides as "solid-solution electrodes" for lithium batteries has directed research towards three-dimensional structures.

Small guest ions, such as hydrogen and the early alkali metals, are able to diffuse through channels formed by interconnected interstices in a framework structure.

The vanadium oxides V_2O_5 and V_6O_{13} [9] are amongst the most studied oxides which undergo reversible topotactic redox reactions. Both these substances can be related, by shearing, to the structure of perovskite ($CaTiO_3$), as can ReO_3 and WO_3.

ReO_3 and WO_3 are formed by corner-sharing MO_6 octahedra which leave cuboctahedral cavities (Fig 1.4). Each cavity shares its square faces with neighbouring cavities, forming interconnected channels in three perpendicular directions.

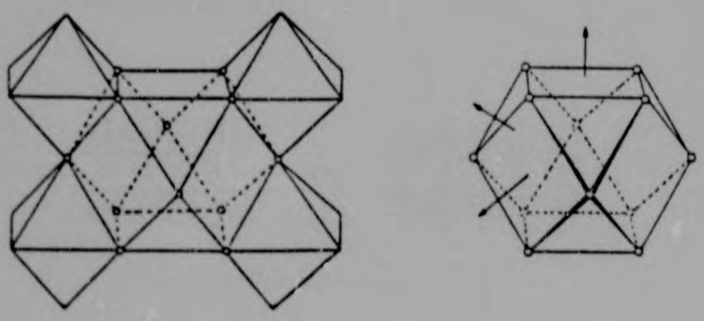


FIG 1.4
Cuboctahedral cavities in ReO_3 and WO_3
Arrows indicate direction of channels [9]

Both ReO_3 and WO_3 undergo intercalation reactions with lithium and other small ions such as hydrogen and sodium.

A combination of corner- and edge-sharing of the MO_6 octahedra can provide other suitable structures for intercalation reactions: a first shear of the ReO_3 structure leads to V_2O_5, a second shear to the V_6O_{13} structure [9] (Fig 1.5).

The insertion of lithium into V_2O_5 has been extensively studied [13,21,22]. The structure contains cavities that form channels in two directions.

One lithium is inserted in each cavitiy, reaching the final composition LiV_2O_5 (Fig. 1.6).

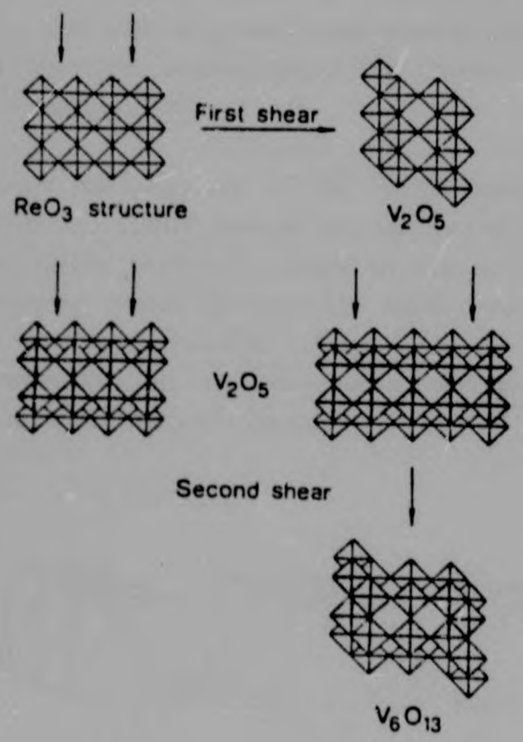


FIG 1.5
Shearing of ReO_3 structure resulting in V_2O_5 and V_6O_{13}
Arrows indicate the shear planes (taken from [16])

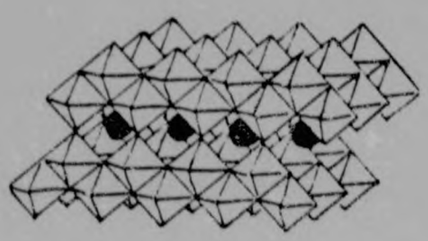


FIG 1.6
Structure of LiV_2O_5 (taken from [23])

In the case of V_6O_{13}, which has a structure similar to that of V_2O_5, but with additional edge-sharing between the octahedra, the final composition of the lithium insertion reaction is $Li_8V_6O_{13}$ [9].

Transition metal oxides of the rutile type and, indeed, rutile (TiO_2) itself undergo lithium intercalation [24,25]. In the rutile structure, characterised by a tetragonally close-packed oxygen lattice with metal ions in octahedral sites, the empty channels, formed by corner- and edge-sharing octahedra, are available for Li diffusion; they allow one-dimensional motion (Fig 1.7).

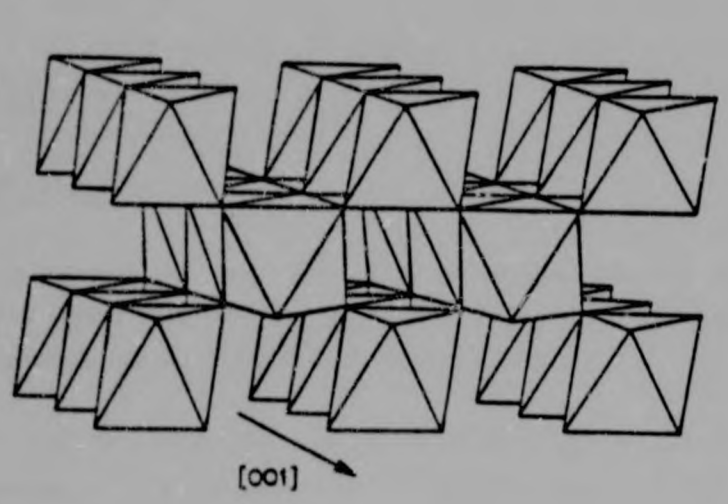


FIG 1.7
Channels in the rutile structure [25]

Several rutile phases reversibly incorporate lithium to varying extents: MnO_2, CrO_2, MoO_2, WO_2, RuO_2, OsO_2, IrO_2 and $MoVO_4$ [25]. The reasons why not all rutile phases undergo the reaction are

not yet fully understood, although electronic conductivity and unit cell volume are known to play a part.

Oxo- and thiospinels are also being studied as possible intercalation cathodes for lithium batteries. The sulphide spinels $CuCo_2S_4$, $CuNi_2S_4$ and $CuFe_2S_4$ reversibly incorporate lithium [26], as do several oxide spinels, amongst which are Fe_3O_4, $LiFe_5O_8$, $LiMn_2O_4$, Mn_3O_4 and Co_3O_4 [27-34]; however, some of these systems are not reversible.

The insertion of lithium into spinels will be dealt with more extensively elsewhere in this work; a brief introduction to this topic is given in section 1.4.

1.2 SPINELS

1.2.1 Definition

Spinels are crystalline compounds with the general formula AB_2X_4, where A,B = metal cations and X = O^{2-}, S^{2-}, Se^{2-}, isomorphous with the mineral spinel $MgAl_2O_4$ (cf section 1.2.3).

Over 230 oxides and sulphides are known to have the spinel structure. Because of the variety of metal cations that are found in spinel compounds, their electrical and magnetic properties can be widely different, and have been studied extensively.

Spinels have found many varied applications, e.g., for refractory materials, ceramics and mineral pigments.

1.2.2 General methods of preparation

Most oxospinels are easily prepared by heating the pure oxides, nitrates or coprecipitated hydroxides, in air, at temperatures varying between 900 °C and 1400 °C.

Thiospinels are generally prepared by heating freshly reduced pure metals with sulphur at high temperatures under vacuum, or by reaction between H_2S or CS_2 and the corresponding oxospinel [35].

1.2.3 The spinel structure

1.2.3.1 Introduction

The structure of spinel ($MgAl_2O_4$) was first described by Bragg in 1915 [36], and has since been the object of numerous studies [37-40].

The crystallographic unit cell contains eight AB_2X_4 formula units. It consists of a cubic close-packed array of anions, in which one eighth of the 64 tetrahedral interstices and one half of the 32 octahedral interstices are occupied by the cations (Fig 1.8, 1.9).

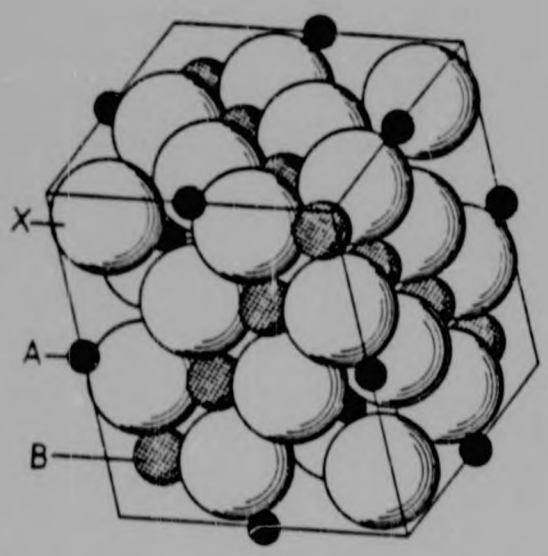
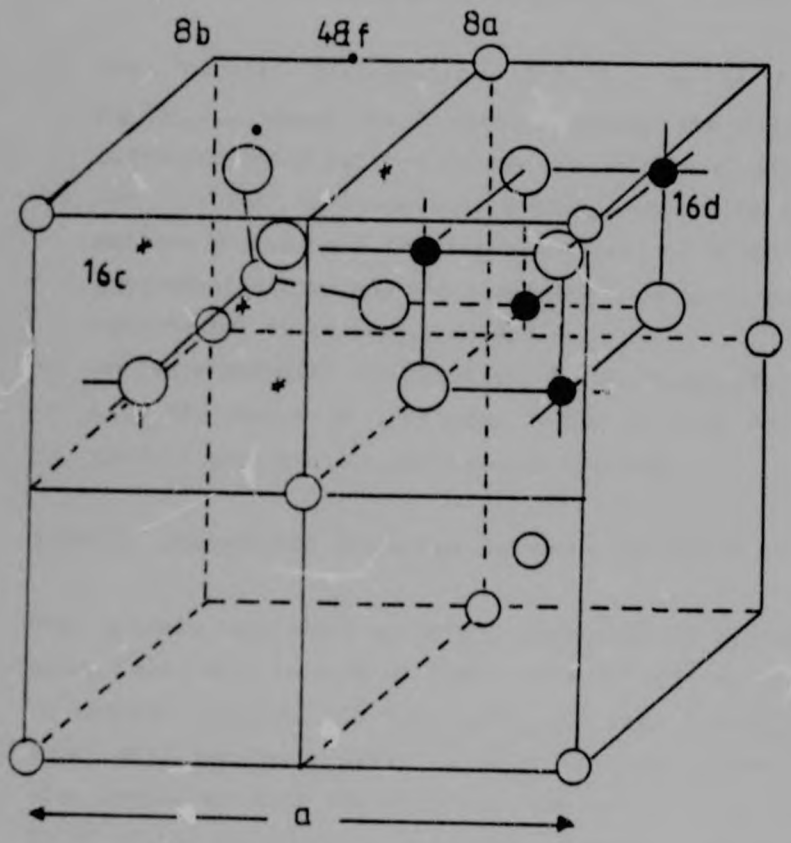


FIG 1.8
Unit cell of the spinel structure (taken from [56])



● A cation
○ B cation
◯ Anion

FIG 1.9
Atomic and interstitial sites in the spinel structure
(Taken from [102])

The occupied tetrahedral sites are called the A sites, the occupied octahedral sites the B sites; the octahedral cations are generally indicated between square brackets, e.g., $A[B_2]X_4$. In a binary spinel $A^{II}B_2^{III}X_4$ three different distributions of the cations are possible:

a) the "normal" distribution, $A[B_2]X_4$, as is found in $Mg[Al_2]O_4$, where the A cations occupy the tetrahedral sites and the B cations occupy the octahedral sites.
b) the "inverse" distribution, $B[AB]X_4$, where the divalent cations A and half the trivalent cations B are in the octahedral sites, and the remaining B cations occupy the tetrahedral sites (e.g., Fe_3O_4).
c) an "intermediate" distribution, $A_{1-\lambda}B_\lambda[A_\lambda B_{2-\lambda}]X_4$, where λ is the degree of inversion (equal to zero for normal spinels and to unity for inverse spinels).

1.2.3.2 Interatomic distances and the u parameter

Most spinels have cubic symmetry, characterised by the space group $Fd\bar{3}m$ [40]. Spinels of lower symmetry will be described in section 1.2.3.3. In this work, the term 'spinel structure' will generally refer to cubic spinels, unless otherwise specified. With the origin of the unit cell at $\bar{3}m$, one-third of the A-cations occupy the tetrahedral 8a positions located at (0.125 0.125 0.125). The B-cations are situated in the 16d positions at (0.5 0.5 0.5), and the anions occupy the 32e sites, with coordinates (x x x).

The exact position of the anions differs slightly from the ideal cubic close-packed structure, and is described by the u parameter. For an ideal structure the 32e position corresponds to (0.25 0.25 0.25), i.e., u = 0.25, when the origin of the unit cell is placed at the symmetry centre $\bar{3}m$. An alternative origin, $\bar{4}3m$ at (-0.125 -0.125 -0.125) is occasionally used for defining the spinel unit cell, in

which case the ideal u parameter has the value of 0.375. In most spinels, however, the anionic lattice is slightly deformed from ideality, although cubic symmetry is maintained; the anions are then situated in a position described by the coordinates (u u u). The parameter u is generally greater than 0.25, although a few spinels are known with u < 0.25.

The distances between cations vary only with the cell parameter a (which depends largely on the radii of the cations), whereas the separation between anions and the bond lengths between cations and anions depend on both the lattice parameter a and the anion positional parameter u (Table 1.1).

TABLE 1.1

Interatomic distances in spinels as a function of "a" and "u" ("u" value with the unit cell origin at the centre of symmetry) [40]

ATOM PAIR	DISTANCE	COMMENTS
A...A	$a\sqrt{3}/4$	tet-tet cation separation
A...B	$a\sqrt{11}/8$	tet-oct cation separation
B...B	$a\sqrt{2}/4$	oct-oct cation separation
A - X	$a\sqrt{3}(u-0.125)$	tet bond
B - X	$a(3u^2-2u+0.375)^{1/2}$	oct bond
X...X	$a\sqrt{2}(2u-0.25)$	tet edge
X...X	$a\sqrt{2}(0.75-2u)$	shared oct edge
X...X	$a(4u^2-2u+0.375)^{1/2}$	unshared oct edge

The occupied 16d octahedral sites share 6 of their edges with other 16d sites, forming a 3-dimensional array, the tetrahedral 8a sites share all four faces with empty 16c interstitial octahedral sites. Each anion at the 32e position has point symmetry 3m and is situated close to one tetrahedral and three octahedral cations (Fig 1.10).

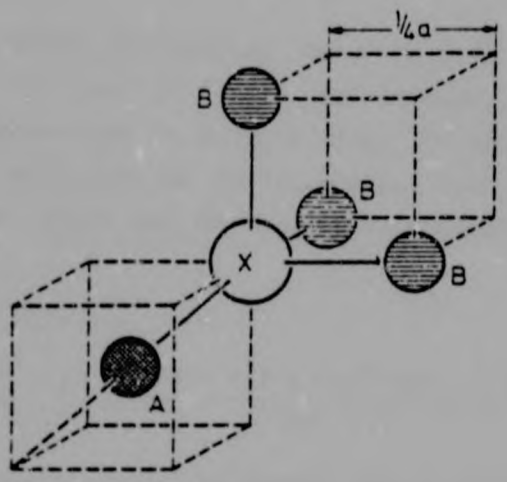


FIG 1.10
Nearest neighbours of the anion (X) in the spinel structure

As u increases above 0.25 the anions move away from the nearest occupied tetrahedral site in a [111] direction; the size of the tetrahedron thus increases, whilst the B octahedra become smaller, and the shared edges between octahedra are shortened.

The value of u therefore reflects the ratio of the radii of the cations in the octahedral and the tetrahedral sites respectively.

Because the bond lengths vary with u, it is possible to determine an upper and a lower limit of u, for a given lattice parameter "a": for a mean lattice parameter a = 8.4 Å for oxide spinels, $0.25<u<0.274$ [40]. If $u<0.25$, the octahedral bond length would be much larger than the tetrahedral bond and the shared edges of the octahedra would be longer than the unshared ones, in contradiction with Pauling's theory on the chemical bond [41]. For $u>0.274$ the structure is destabilised, because the shared edges of the octahedra decrease to values at which the repulsion forces between

anions become increasingly important [40]. These calculated limits for u are in fairly good agreement with the observed anion parameters in oxide spinels. In conclusion, the ratio of the octahedral to the tetrahedral bond lengths affects u, and the latter can be calculated according to the expression:

$$u = \frac{R^2/4 - 2/3 + (11R^2/48 - 1/18)^{\frac{1}{2}}}{2R^2 - 2} \qquad (1.1)$$

$$\text{where } R = \frac{\text{octahedral cation radius}}{\text{tetrahedral cation radius}}$$

1.2.3.3 **Lower symmetry spinels**

Although most spinels belong to the cubic space group Fd3m, the symmetry may be lowered by a distortion of the lattice or by the presence of superstructures.

1.2.3.3.i Superstructures

When two or more types of cation occupy the tetrahedral or the octahedral sites, long-range cation ordering may occur, lowering the overall cubic symmetry of the spinel. Many of these superstructures exist at low temperatures; at high temperatures a random arrangement of the cations is preferred.

A few examples of superstructures are:

Fe_3O_4 (magnetite). Fe_3O_4 at T>120K is an inverse cubic spinel, where the ferrous and ferric ions are randomly arranged over the 16d sites. At T<120K, where the Fe^{2+} and Fe^{3+} cations display an ordered distribution on the 16d sites, the structure becomes monoclinic [42,43].

γ-Fe_2O_3. γ-Fe_2O_3 has a spinel structure, with vacancies on the octahedral sites: $Fe^{+3}[\ \square\ _{1/3}Fe^{+3}{}_{5/3}]O_4$, where $\square$ denotes a vacancy. Due to the ordering of the Fe^{+3} ions and the vacancies on the octahedral sites, the structure adopts tetragonal symmetry [44] and is characterised by the space group $P4_3\ 2_1\ 2$ [45]. A phase transformation occurs at T=1000K, when the structure becomes cubic [46]. At this temperature the cations are randomly distributed between the octahedral and the tetrahedral sites.

$LiAl_5O_8$ and $LiFe_5O_8$. These two compounds are isostructural, having the cubic space group $P4_332$. Long-range order exists on the octahedral sites which are occupied by two types of cations: $Al_2[LiAl_3]O_8$ and $Fe_2[LiFe_3]O_8$ [47].

$LiGa[Cr_4]O_8$. In this structure the lithium and gallium atoms are ordered in the tetrahedral positions resulting in a crystal with the symmetry of the cubic space group $F\bar{4}3m$ [46]. A disordered form of $LiGa[Cr_4]O_8$, with random distribution of lithium and gallium ions, exists for T>1323K [46].

1.2.3.3. ii Lattice distortion

Many spinels (e.g., Mn_3O_4, $CuFe_2O_4$, $CuCr_2O_4$, $ZnMn_2O_4$) have a tetragonal crystal structure.

Hausmannite (Mn_3O_4) crystallises in the tetragonal space group $I4_1/amd$ and can be described as a spinel elongated in the [001] direction.

The c/a ratio in tetragonally distorted spinels may be <1 as in $CuCr_2O_4$ (c/a = 0.91), or >1 as in Mn_3O_4 (c/a = 1.16). The origin of the distortion was first explained by Goodenough and Loeb [48], who examined the role of covalence of transition metal ions, and concluded that the distortion was due to covalent bonding between the anions and the cations located either in the tetrahedral or the octahedral sites.

Dunitz and Orgel [49] discussed the structure from the point of view of crystal field theory, and attributed the distortion to the Jahn-Teller effect. This theory has since been widely accepted and used to explain the distortion found in many spinels, e.g., in manganites [50], on account of the d^4 Mn^{3+} ion, in which the e_g orbitals are not energetically degenerate. In the copper spinels $CuFe_2O_4$, $CuCr_2O_4$ and their intermediates $CuFe_{2-t}Cr_tO_4$ $(0<t<2)$ [51], the lattice is distorted due to the presence of the d^9 Cu^{2+} cation.

1.2.4 Cation distribution

1.2.4.1 Introduction

As has already been mentioned in section 1.2.3.1, three different cation distributions are possible in a binary spinel:

- the normal distribution $A[B_2]X_4$
- the inverse distribution $B[AB]X_4$
- the intermediate distribution $A_{1-\lambda}B_\lambda[A_\lambda B_{2-\lambda}]X_4$, where λ is the degree of inversion $(0<\lambda<1)$.

The cation distribution affects the structural, electrical and magnetic properties of spinel oxides, and has therefore been extensively studied.

1.2.4.2 Experimental determination

Cation distribution in spinels has been determined experimentally mainly by X-ray powder diffraction, and, in some cases, by Mössbauer spectroscopy, e.g., in Co and Fe spinels [52]. Powder X-ray diffraction is a satisfactory method if the cations have sufficiently different scattering factors; if this is not the case and if their relative scattering cross-section for neutrons is very different, it is possible to use neutron powder diffraction techniques.

Both the anion parameter u and the degree of inversion λ are thus determined simultaneously. Several methods have been used to this purpose, amongst which the most common are:

a) Bertaut's method [53], which consists of comparing measured (I_{obs}) and calculated intensity (I_{calc}) ratios of selected reflections, at similar 2θ values, that are influenced in a different way by changes in the parameters u and λ.

b) Fuhurashi's method [54], which examines the linearity of the plot:

$$\ln(I_{obs}/I_{calc}) = \ln K - 2B \sin^2\theta/\lambda^2 \qquad (1.2)$$

where $I_{calc} = |F^2|Lpm$ (1.3)

with K = scale factor
B = temperature factor
θ = angle of diffraction
λ = radiation wavelength
F = structure factor
Lp = Lorentz-polarisation factor
m = multiplicity

c) The R-factor method, where the best correlation between calculated and observed intensities is measured by the factor:

$$R = \frac{\sum |I_{obs} - I_{calc}|}{\sum I_{obs}} \qquad (1.4)$$

where $I_{calc} = Ke^{-2B(\sin\theta/\lambda)^2} \cdot |F^2|Lpm$ (1.5)

The spinel parameters u and λ may be determined with great precision if the three methods are used in conjunction with one another [55].

1.2.4.3 Theoretical models

In 1947, for the first time, an attempt was made to predict cation distribution in spinels by assuming a purely electrostatic model and calculating the Madelung lattice energies for both normal and inverse structures [56]. Further calculations [57] indicated that $A^{2+}B_2^{3+}O_4$ (known as 2:3 spinels) favoured the normal structure, whereas $A^{4+}B_2^{2+}O_4$ (4:2 spinels) were more stable with an inverse structure.

As more spinel structures were determined experimentally, it became obvious that this theory overlooked other important contributions.

An alternative approach was used by McClure [58], Dunitz and Orgel [59]. They explained the preference for octahedral or tetrahedral sites using crystal field theory. The coordinating oxygens split the d orbitals of the cations, making some cations more stable and others less stable in a tetrahedral or an octahedral environment. The cations will occupy the sites which afford the maximum crystal field stabilisation energy (CFSE).

Very similar results were obtained by Cotton [60] with ligand field theory: normal and inverse structures were accounted for by considering the interactions between the transition metal d orbitals and the ligand field, using molecular orbital theory.

Although these theories predict the structures of a great number of spinels correctly, they cannot be applied univer-

sally, either because the predicted structure is occasionally incorrect, or because the normal and inverse structures are equivalent in terms of these models.

Several authors have recalculated the Madelung constants for spinels [61,62], and have found that the difference in electrostatic energy between the normal and the inverse structure is often much larger than the predicted changes in CFSE [63].

More recently, in a comprehensive study of the thermodynamics of spinels, Popov and Levitskii [64] discussed the correlation between electrostatic energies and cation distribution. The Madelung constant α is a function of the anion parameter u and of the charge in the tetrahedral site q_t, which in turn depends on the degree of inversion λ; there is therefore a relationship between the Madelung constant and the cation distribution.

Popov and Levitskii [64] stated that 2:3 spinels are normal if the derivative $\frac{\partial \alpha}{\partial q_t} < 0$; inverse if $\frac{\partial \alpha}{\partial q_t} > 0$; the reverse is true for 4:2 spinels.

These predictions coincide satisfactorily with experimental data, except in the proximity of the u value that corresponds to the condition α (normal) = α (inverse). For these values, Popov and Levitskii [64] conclude that other contributions to the energy of the lattice, i.e., polarisation energy or stabilisation energy, mask the effect of the electrostatic energy.

Prior to the advent of crystal field theory, Goodenough and Loeb [48] suggested that a partial covalent bonding model could account for cation distribution in spinels.

Shubin et al [65], stating that previous theories were insufficient because they did not allow for partial covalence, calculated a cation distribution preference energy. This energy was obtained by computing the octahedral and the tetrahedral fragments separately, using the MO-LCAO method (Molecular Orbital - Linear Combination of Atomic Orbitals theory), maintaining self-consistency of the charge and of the electron configuration of the central atom.

The normal spinel structure $A[B_2]O_4$ was split into one tetrahedral fragment AO_4 and two octahedral fragments BO_6, and the inverse structure $B[AB]O_4$ was similarly divided into the fragments BO_4, AO_6 and BO_6.

The preferred structure could then be estimated from the difference between the energies E_{norm} and E_{inv}, where:

$$E_{norm} = E(AO_4) + 2E(BO_6)$$
$$E_{inv} = E(BO_4) + E(AO_6) + E(BO_6)$$

The results obtained by this method coincide with experimentally determined distributions.

This approach, coupled with the Madelung constant method, probably deserves further investigation.

1.3 STRUCTURE OF $LiMO_2$ COMPOUNDS (M=V,Co,Cr,Ni)

The oxides $LiMO_2$ (M=V,Co,Cr and Ni) are isomorphous and crystallise in the trigonal space group $R\bar{3}m(D^5_{3d})$. The unit cell contains three $LiMO_2$ units.

The anions form a cubic close-packed array, in which the lithium and the transition metal cations are situated in alternate layers, in octahedral sites. The structure can thus be seen as a

series of parallel planes, consisting of Li^+, M^{3+} and O^{2-} ions respectively, arranged according tc the sequence ...O-Li-O-M-O-Li... etc. (Fig 1.11).

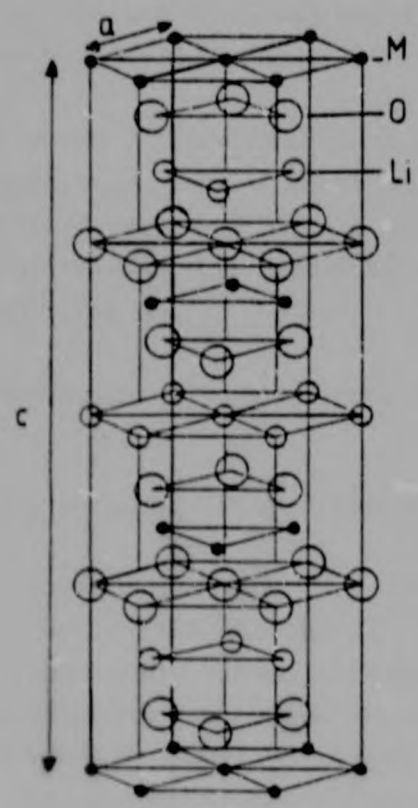


FIG 1.11
Structure of $LiMO_2$ (M = V, Co, Cr, Ni)

When referred to hexagonal axes, with the origin of the unit cell at the centre of symmetry ($\bar{3}$), the atoms occupy the following positions:

ATOM	POSITION	COORDINATES
Li^+	3a	(0,0,0)
M^{3+}	3b	(0,0,0.5)
O^{2-}	6c	(0,0,z)

In these $LiMO_2$ compounds all the octahedra of the cubic close-packed array are occupied by the cations.

There are two sets of empty tetrahedral sites which are crystallographically non-equivalent, both of which are defined by the 6c positions. In a cubic close-packing all the octahedra share edges, as do the tetrahedra; the octahedral sites share faces with the tetrahedral sites.

In this work, the extraction of lithium from $LiVO_2$ is studied.

1.4 LITHIUM INSERTION/EXTRACTION REACTIONS WITH OXO-SPINELS

Over the past few years it has been shown that lithium can be accommodated into oxo- and thiospinels (cf section 1.1.5.3). Furthermore, lithium-containing halospinels have also been investigated as solid electrolytes for lithium cells [66-71]; although their ionic conductivity is generally not sufficiently high for practical use at ambient temperature, they demonstrate that lithium-ion transport through the spinel structure is possible.

This work, however, will deal exclusively with topochemical reactions of lithium with oxo-spinels. A brief introduction to this topic is given in the next sections.

1.4.1 General

Ambient temperature lithiation of oxo-spinels was first reported in 1982, when $Li_xFe_3O_4$ was prepared both by chemical and electrochemical techniques [28]. Since then, a number of spinels

have been lithiated; amongst these are Mn_3O_4, Co_3O_4, $LiFe_5O_8$, several manganite spinels of the type MMn_2O_4, zinc spinels with the general formula ZnB_2O_4 and ferrite spinels with the formula $M^{2+}Fe_2O_4$ [28,31-34,72,73].

Lithium has also been inserted into and/or extracted from lithium-containing spinels, where the Li^+ cations are situated in the A-sites, such as $LiMn_2O_4$, $LiTi_2O_4$, $LiMnRu_{1-x}Ti_xO_4$ $(0<x<1)$ and $Li_{1-x}Cu_xMnRuO_4$ $(x<0.65)$ [33,74-80].

Topochemical reactions of lithium with oxide spinels have been examined predominantly from a structural and mechanistic point of view; preliminary electrochemical studies have been carried out on some systems. A review of this subject was published recently [81].

Spinel lithiation mechanisms and structures of the products will be discussed in detail in the course of this work: they will therefore not be presented here. However, a brief description of the interstitial sites in spinels follows, as it is fundamental in order to understand the processes investigated throughout this work.

1.4.2 Interstitial sites in spinels

As it has already been noted, in cubic spinels, with prototypic symmetry Fd3m, the tetrahedral 8a and the octahedral 16d sites are occupied by the A and B cations respectively (Figs. 1.8 - 9).

Because the 8a sites are the most distant positions from the 16d sites, they are energetically the most favourable for the A cations.

Insertion of small guest ions into a host is possible only if energetically favourable sites are available in the lattice, where relatively little energy would be required for insertion to occur.

Apart from the occupied 8a and 16d sites, the spinel structure has several vacant interstices, viz. the tetrahedral 8b and 48f and the octahedral 16c sites. Each tetrahedral 8b site shares faces with 4 occupied 16d octahedra; each 48f site shares faces with two occupied 16d and two unoccupied 16c octahedral sites. The proximity of the B cations makes insertion prohibitive in the 8b sites, difficult in the 48f sites.

The empty 16c octahedra share faces with six vacant 48f and two occupied 8a tetrahedra. Although a priori one might exclude the possibility of inserting guest ions into the 16c interstices, because of the repulsion originating from the A cations in the neighbouring 8a sites, it has been found that lithium can be inserted into the 16c sites of the spinel structure, causing part or all of the A cations to migrate to these sites [28,33].

The $[B_2]X_4$ framework of the spinel structure thus provides a three-dimensional network of channels, consisting of the 8a and 16c sites, through which small cations, such as lithium, can diffuse [28].

1.4.3 The $Li[M_2]O_4$ (M = Ti,V,Mn) Spinels

The spinels $Li[M_2]O_4$ (M = Ti,V,Mn) are of particular interest as potential electrodes for primary or secondary lithium batteries. Firstly, they are mixed valence compounds, and therefore electronic conductors. Secondly, lithium can not only be inserted into, but also extracted from these compounds. This is of particular importance in view of their potential use in lithium batteries, as it widens the compositional range of the working electrode, thereby enhancing its capacity. Finally, the $Li[M_2]O_4$ spinels should offer increased mobility through the interstitial space of the $[B_2]X_4$ framework, when compared to other AB_2X_4 spinels, where A is a transition metal cation, e.g. Fe_3O_4, Co_3O_4, Mn_3O_4 or $LiFe_5O_8$. In the latter category of spinels, lithium diffusion is hindered at all stages of the reaction by the pres-

ence of the relatively heavy, large transition metal cations present in the interstitial space of the $[B_2]X_4$ framework, which comprises the 8a tetrahedra and the 16c octahedra (cf section 1.4.2). In the $Li[M_2]O_4$ compounds, where only lithium cations occupy the A sites, maximum lithium mobility should be attained.

Topochemical reactions of lithium with the spinel LiV_2O_4 will be studied in this work.

1.5 AIM OF THIS WORK

In this work, the topochemical reactions between lithium and transition metal oxides will be studied. In particular, lithium insertion into, and extraction from spinels will be examined both theoretically and experimentally.

From a theoretical point of view, the electrostatic energy variations which occur during lithium insertion into spinels will be calculated; the compounds Mn_3O_4 and $LiMn_2O_4$ are chosen as representative of the two main mechanisms by which lithium can be inserted into oxo-spinels.

The experimental studies in this work will concern insertion and extraction reactions of lithium with LiV_2O_4 and $LiVO_2$.

Topochemical reactions of lithium with several vanadium oxides have been extensively studied during the past decade [9,22,82-84]. The pentavalent vanadium compounds V_2O_5 and particularly V_6O_{13} show promise as electrode materials for lithium batteries (cf section 1.1.5.3) [21,22,85-93]. More recently other vanadium oxides, e.g. $VO_2(B)$ and $Li_{1+x}V_3O_8$, have been investigated [93-99].

The lithium vanadium spinel LiV_2O_4, with tri- and tetravalent vanadium ions, is isostructural with the spinels $LiMn_2O_4$ and

$LiTi_2O_4$. The advantages of the $Li[M_2]O_4$ spinels over other compounds with the spinel structure have already been discussed in section 1.4.3.

Recent studies have shown that the spinel $LiMn_2O_4$ and its derivatives $Li_{1\pm x}Mn_2O_4$ $(0<x<1)$ can be used as cathodes in lithium batteries [33,74-76,100]. In fact, although the mechanism has not yet been fully elucidated, there are good indications that the reaction of the commercial $Li|\gamma\text{-}MnO_2$ batteries may involve a transformation of $\gamma\text{-}MnO_2$ to the spinel structure [102,103].

The promising results obtained with $LiMn_2O_4$ have prompted the study of topochemical reactions of lithium with the isomorphous spinels $Li[M_2]O_4$ where M = Ti, V.

Lithium insertion/extraction reactions with LiV_2O_4 will be studied from a structural and an electrochemical point of view, and will be compared with the isomorphous compounds $LiTi_2O_4$ and $LiMn_2O_4$.

A method for stabilising the spinel $[B_2]X_4$ framework of delithiated $Li_{1-x}V_2O_4$ will also be investigated.

Lithium extraction from the layered compound $LiVO_2$ will also be structurally and electrochemically characterised. One of the metastable products of this reaction, $Li_{0.5}VO_2$, will be used to develop a new route for the synthesis of the lithium spinel LiV_2O_4.

CHAPTER 2

OVERVIEW OF EXPERIMENTAL TECHNIQUES

A number of instrumental techniques were used throughout this work to study reactions and new compounds.

The structures of novel materials were characterised by powder X-ray diffraction, phase transformations were studied by differential scanning calorimetry, and various aspects of the electrochemical reactions were examined using several electrochemical methods.

The general principles and the instrumentation of these techniques will be briefly presented in this chapter.

2.1 POWDER X-RAY DIFFRACTION

2.1.1 History of X-ray diffraction

The discovery of X-rays by Roentgen dates back to 1895; although the nature of the radiation was still unknown, it was used soon afterwards for medical purposes. The nature of X-rays was understood only 17 years later, when X-ray diffraction by crystalline materials was discovered.

The first X-ray diffraction experiment was performed on a single crystal by von Laue in 1912; in the same year, W L Bragg gave a simple interpretation of the phenomenon.

X-rays are a form of electromagnetic radiation of a similar wavelength as the interatomic distance in crystals, and can therefore be diffracted by planes of atoms.

2.1.2 The Bragg Law

Diffraction, as opposed to reflection, is concerned with the bulk of the crystal and is not a phenomenon limited to the surface. Furthermore, if a monochromatic beam is used, diffraction is observed only for certain well-defined angles of incidence.

Although in rigorous terms it is incorrect to call the diffracted beam a reflection, the diffraction phenomenon can be interpreted in terms of a simple reflection from a set of crystallographic planes.

Diffraction can be described as a scattering phenomenon: although atoms scatter radiation in every direction, diffraction is observed only if the scattered rays are in phase, i.e., if they reinforce one another constructively and do not cancel each other out. This basic condition was expressed mathematically by W L Bragg, and is known as the Bragg law.

X-ray diffraction by a set of parallel planes in a crystal can be illustrated simply as in Fig 2.1.

The rays diffracted by two planes will be in phase if the difference in length of their paths (δ) is equal to a multiple of the radiation wavelength (λ):

$$\delta = n\lambda \qquad \text{where } n = \text{integer} \qquad (2.1)$$

In Fig 2.1 the difference in path length is expressed by:

$$\delta = AB + AC = 2AB = 2d.\sin\theta \qquad (2.2)$$

where θ = angle of incidence

d = interplanar spacing

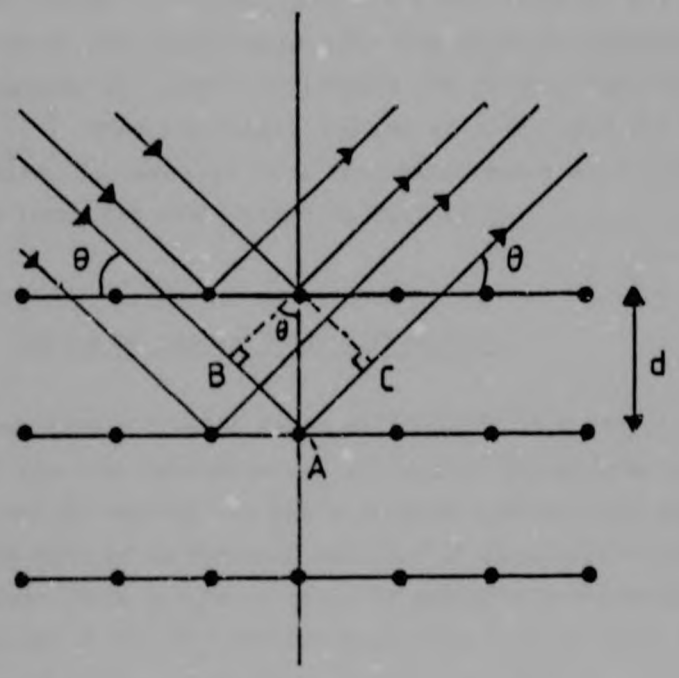


FIG 2.1
Diffraction by planes of atoms in a crystal

The condition necessary for diffraction to occur is thus:

$$n\lambda = 2d.\sin\theta \qquad \text{Bragg Law} \qquad (2.3)$$

The integer n expresses the order of the reflection: since an nth order reflection from an (hkl) plane can be considered a first order reflection from a (nh nk nl) plane, it is generally more convenient to take n=1, giving equation 2.3 the more simple form:

$$\lambda = 2d.\sin\theta \qquad (2.4)$$

Each plane in a crystal is defined by its Miller indices hkl.

Miller indices of a plane are the reciprocals of the intercepts which the plane makes with the crystallographic axes; for example, if a plane intercepts the crystallographic axes at $\frac{a}{h}, \frac{b}{k}, \frac{c}{l}$ then the Miller indices of that plane are h k l. If a plane is parallel to a crystallographic axis, then the Miller index for that direction will be 0.

2.1.3 Choice of powder X-ray diffraction

Although single crystal X-ray diffraction is a very powerful method for the determination of crystal structures and has been used to resolve extremely complex systems, its application is limited by the availability of single crystals. In instances where single crystals of material are unavailable, the powder X-ray diffraction technique must be used to determine the atomic structure of the compound.

Single crystals of intercalated compounds are particularly difficult to obtain, since the preparation of these products often results in the break-up of the starting material into very small particles. Furthermore, the products are often metastable, and subsequent treatment, for example heat-treatment, might alter the structure. Powder X-ray diffraction is therefore one of the most widely used tools for the structural analysis of these compounds.

In powder X-ray diffraction, the sample is in the form of a fine powder; a monochromatic source of X-rays is used, and the angle of the incident beam (θ) is varied.

The random distribution of the particles ensures that the scattering of X-rays from all the atomic planes is represented in the powder X-ray diffraction pattern.

2.1.4 Structure determination by powder X-ray diffraction

Structural information on a compound may be obtained from both the position and the relative intensity of each reflection.

2.1.4.1 **Symmetry of the unit cell and lattice constants**

The position of the reflection, given by the angle of incidence of the beam, and generally expressed in 2θ, can be related to the interplanar spacing (d) according to the Bragg Law (Eq. 2.3).

The interplanar spacings of a crystal are related to the indices of the plane and to the lattice constants. Different functions apply according to the symmetry of the unit cell; expressions for a few systems are listed below.

- Cubic symmetry:

$$\frac{1}{d^2} = \frac{h^2 + k^2 + l^2}{a^2} \qquad (2.5)$$

- Tetragonal symmetry:

$$\frac{1}{d^2} = \frac{h^2 + k^2}{a^2} + \frac{l^2}{c^2} \qquad (2.6)$$

- Hexagonal symmetry:

$$\frac{1}{d^2} = \frac{4}{3}\left(\frac{h^2 + hk + k^2}{a^2}\right) + \frac{l^2}{c^2} \qquad (2.7)$$

- Orthorhombic symmetry:

$$\frac{1}{d^2} = \frac{h^2}{a^2} + \frac{k^2}{b^2} + \frac{l^2}{c^2} \qquad (2.8)$$

The position and number of reflections thus give information on the shape and size of the unit cell.

2.1.4.2 **Atomic positions**

The relative intensities of the reflections can be used to determine the position of the individual atoms within the unit cell : several factors, which will be briefly described here, affect the relative intensity of a powder X-ray diffraction line.

a) The structure factor

The structure factor, F, is basically an expression for the wave scattered by the atoms in a plane (h k l) within the unit cell, and is specific to a given structure. The determination of a crystal structure by X-ray diffraction depends mainly on this term.

A wave can be described by combining its amplitude A and phase Φ according to the expression $A.e^{i\Phi}$.

The structure factor is obtained by summing the contributions of all the atoms (N) in a plane of the unit cell; they are characterised by two terms that describe their amplitude and phase.

The first term is the atomic scattering factor, f, which expresses the amplitude of the wave scattered by the atom. The atomic scattering factor is directly proportional to the number of electrons of a given atom (or ion), and decreases as the quantity $\frac{\sin\theta}{\lambda}$ increases. A comprehensive list of atomic scattering factors is given in the "International Tables for X-ray Crystallography" [103].

The second term of the structure factor expresses the phase of the wave scattered by each atom, and is given by the expression:

$$\Phi = 2\pi(hu + kv + lw) \qquad (2.9)$$

where hkl = indices of the plane
uvw = fractional coordinates of the atom

The wave scattered by each atom is thus defined by the expression:

$$Ae^{i\Phi} = fe^{2\pi i(hu+kv+lw)} \qquad (2.10)$$

Finally, the structure factor is given by the expression:

$$F_{hkl} = \sum_{n=1}^{N} f_n \cdot e^{2\pi i(hu_n + kv_n + lw_n)} \qquad (2.11)$$

The intensity of the beam diffracted by a plane (hkl) is proportional to $|F_{hkl}|^2$.

b) Other factors affecting the relative intensities

Several other factors must be included in the calculation of the intensity of a diffracted beam. Some of these are strictly related to the atoms and the structure of the crystal, others are derived from geometrical considerations.

- The multiplicity factor, p, depends on the symmetry of the crystal, and expresses the number of planes with the same d spacing, but with different Miller indices (hkl).

- The temperature factor takes into account the thermal vibration of the atoms in the crystal. Thermal vibration decreases the relative intensity of the diffracted beam, since it displaces the atoms from an ideal

plane; the effect increases at high temperature and for high θ angles.

The temperature factor is given by the quantity e^{-2M}, where M depends on the average displacement, $\bar{u}$, of the atom and the angle θ:

$$M = 2\pi^2\left(\frac{\bar{u}^2}{d^2}\right) = 8\pi^2\overline{u^2}\left(\frac{\sin\theta}{\lambda}\right)^2 = B\left(\frac{\sin\theta}{\lambda}\right)^2 \quad (2.12)$$

B $(=8\pi^2\bar{u}^2)$ is the isotropic temperature factor, and is generally expressed in $Å^2$; λ is the radiation wavelength in Å.

- The polarisation factor is derived from the Thomson equation (eq. 2.13), which expresses the intensity of an X-ray beam scattered by an electron.

The intensity of the scattered beam, at a point P, is a function of the distance r between P and the electron and of the angle of diffraction θ:

$$I_p = I_o \frac{K}{r^2}\left(\frac{1 + \cos^2 2\theta}{2}\right) \quad (2.13)$$

where I_p = intensity at a point P
I_o = intensity of the incident beam
K = constant
r,θ as defined in the text

The expression in brackets is known as the polarisation factor. It is derived from the fact that the incident beam is unpolarised and can be divided into two polarised components, whose scattered intensities differ and vary with θ.

- The Lorentz factor comprises a number of effects due to geometrical considerations, which cause some diffraction to be observed at angles that differ slightly from the Bragg angle θ.

  The Lorentz factor is a function of θ and is given by the expression:

$$\text{Lorentz factor} = \frac{1}{4\sin^2\theta\cos\theta} \qquad (2.14)$$

  The Lorentz and the polarisation factors are usually expressed in a combined form (eq. 2.15), omitting the constant factor $\frac{1}{8}$:

$$\text{Lorentz-polarisation factor} = \frac{1 + \cos^2 2\theta}{\sin^2\theta\cos\theta} \qquad (2.15)$$

- The absorption factor, A, takes into account the absorption of the beam by the sample. For the powder diffractometer, with flat-plate geometry, this quantity is constant ($A=0.5\mu$, where μ = linear absorption coefficient) and independent of θ. It was therefore omitted in this work. In a Debye-Scherrer camera, it is θ-dependent and increases as θ increases.

Summing up, the relative intensity of a reflection obtained with a diffractometer is given by equation 2.16:

$$I = |F|^2 \cdot p \cdot \left(\frac{1 + \cos^2 2\theta}{\sin^2\theta\cos\theta}\right) \cdot e^{-2M} \qquad (2.16)$$

Clearly, structural variations are mainly reflected by the structure factor, in particular by the exponential term, which contains the atomic fractional coordinates (uvw).

The contributions of selected atom positions to the intensities of various reflections for the space-groups studied in this work are given in the Appendix.

Structural analyses are generally obtained by comparing the normalised calculated and observed intensities of possible models (the former multiplied by a scale factor, in order to have a comparable scale). During structure refinements by least-square methods, site occupancies, fractional coordinates and temperature factors are varied until the best fit between calculated and observed intensities is obtained.

In this work, the goodness of the fit between observed and calculated intensity data was measured by the general reliability factor R, calculated after each refinement:

$$R = \frac{\sum (I_{obs} - I_{calc})}{\sum I_{obs}} \qquad (2.17)$$

where I_{obs} = observed intensity
I_{calc} = calculated intensity

2.1.5 Instrumentation : the diffractometer

A method for powder X-ray diffraction was first developed by Debye and Scherrer in 1916.

The Debye-Scherrer camera consists of a cylindrical chamber into which the incident beam is introduced through a collimator. The sample is placed in the cylinder axis, and a film, situated in the internal edge of the cylinder, is used to detect the diffracted X-rays.

Several other cameras now exist, amongst which a widely used version is the Guinier camera; it can be described as a focusing camera with a focusing monochromator, and has the advantage of a better resolution than the Debye-Scherrer camera. Details of the construction of these and other cameras are given in reference 104.

In this work, powder X-ray diffraction was carried out using a conventional flat-plate diffractometer. Commercial diffractometers were developed in the late 1940's.

The geometry of the diffractometer is basically identical to that of the Debye-Scherrer camera; the photographic film is substituted by an electronic counter which detects the diffracted X-rays.

A diagram of the diffractometer assembly is shown in Fig 2.2:

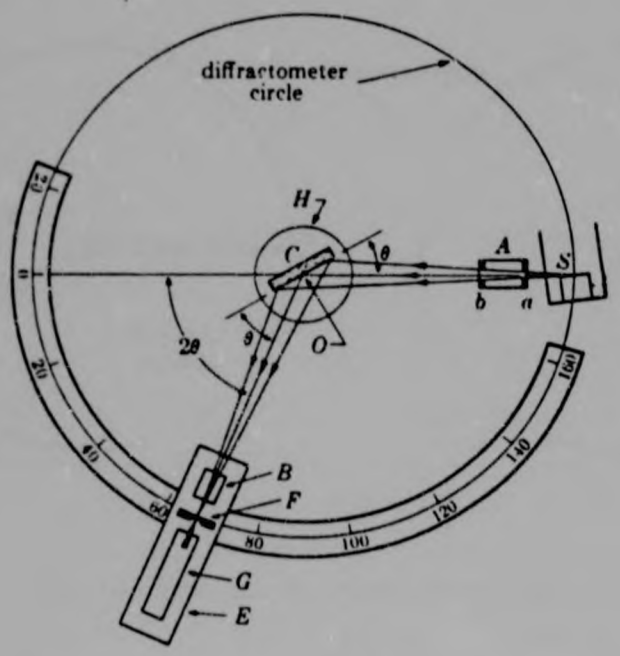


FIG 2.2
The diffractometer assembly (taken from [104])

The beam originates from the X-ray source S, placed on the diffractometer circle, and passes through a series of slits (a,A,b) before it reaches the sample C. The sample is mounted on a glass plate, and must be absolutely flat in order to obtain maximum precision.

The component H, which holds the sample in position, rotates about the axis O, forming an angle of θ with respect to the incident beam.

During operation, the components H and E rotate simultaneously: whilst E must rotate in order to allow the detector to scan the full range of 2θ values, H rotates in order to ensure good focusing conditions. Focusing is obtained by maintaining the source S, the receiving slit F and the sample on the focusing circle (Fig 2.3): this is achieved by rotating the sample about the axis O.

FIG 2.3
The focusing circle (taken from [104])

The slits A and B are known as Soller slits, and consist of several long, thin, metal plates, parallel to the plane of the diffractometer circle, which eliminate, to a large extent, X-rays which diverge excessively from the plane.

Slits a and b, which are situated immediately before and after the Soller slit A, define the divergence of the beam. The detector G is generally a proportional or a scintillation counter.

A filter is usually placed before the receiving slit F, in order to cut out the K_β line and decrease the background radiation.

In modern diffractometers, a monochromator is used instead of a filter and is situated between the receiving slit and the detector. Monochromation is normally achieved from a single crystal, for example, of graphite.

The major advantage of a diffractometer over a camera is that with the former both the position and the relative intensity of the reflection are obtained simultaneously, in a single-step operation, leading to greater accuracy than that obtained with a camera. Furthermore, the diffractometer is less time-consuming since it does not require the development of a film.

2.2 DIFFERENTIAL SCANNING CALORIMETRY (DSC)

2.2.1 Principle

When a substance undergoes a change of physical state, such as fusion or a structural transformation, a certain amount of energy, in the form of heat, is either liberated or absorbed by the system. In differential thermal methods, i.e., differential thermal analysis (DTA) and differential scanning calorimetry (DSC), the difference in enthalpy change between the sample to be analysed and a reference material is recorded when both materials are heated.

In differential scanning calorimetry, the sample and the reference pan are heated by separate heaters. The temperature of the pans is regulated by two circuits. Whilst one system controls the heating or cooling rate, the second circuit adjusts the temperature of one of the pans whenever a temperature difference, due to an endo- or exothermic reaction, occurs. The two pans are thus at an identical temperature at all times.

The power which is necessary to maintain the two pans at an identical temperature is proportional to the enthalpy change, which is recorded as a function of temperature.

The DSC method, which measures an enthalpy variation, is more accurate and sensitive than the DTA method, which records a difference in temperature between two pans heated by a single heater.

The DTA method allows the determination of the endo- or exothermic nature of the transition and the temperature at which the latter takes place.

The DSC method is an improved technique, since it also allows the determination of specific heats and enthalpies of chemical and physical transformations.

2.2.2 Instrumentation

A schematic representation of the DSC heating system is given in Fig 2.4; the sample and reference pans are placed in a cell equipped with separate heaters. Thermocouples measure the temperature of the base of each pan.

Samples and reference materials are generally placed in aluminium pans closed with a tight-fitting lid. If the sample is to be heated under an inert atmosphere, special pans, in aluminium or other materials, which can be hermetically sealed, are used.

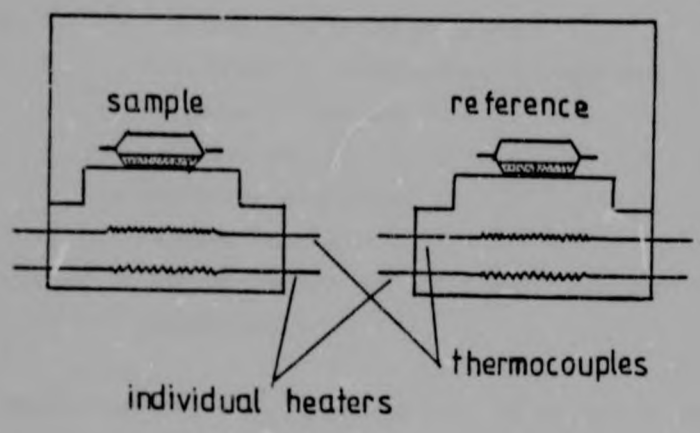


FIG 2.4
The DSC heating system

2.3 THERMODYNAMICS OF ELECTROCHEMICAL CELLS: ELECTROCHEMICAL CURVES

In the course of this work, the electrochemical curve of several systems is determined. The electrochemical curve is obtained by measuring the open-circuit voltage of a cell at equilibrium for different compositions of the working electrode.

In the case of reversible electrochemical systems, a number of thermodynamic relationships are applicable. They can be used to interpret the shape of the electrochemical curve and to obtain thermodynamic quantities for a given system.

The potential of an electrochemical cell E [Volts] is given by the Nernst equation:

$$E = E_o - \frac{RT}{nF} \cdot \ln \frac{[Ox]}{[Red]} \qquad (2.18)$$

where E_o = standard electrode potential [V]

R = k.N, where k is Boltzmann's constant, N is Avogadro's constant

T = temperature [K]

n = number of electrons

F = Faraday constant

[Ox][Red] = concentration of oxidised, reduced species respectively.

The Nernst potential E, given above, is measured when the system is at equilibrium and corresponds to the open-circuit voltage (o.c.v) of the cell.

The reversible work which can be drawn from an electrochemical system, at constant temperature and pressure, is given by the Gibbs free energy of the reaction ($\Delta_r G$). The Gibbs free energy is related to the Nernst potential (E) and to the composition of the working electrode (x) by the expression:

$$\Delta_r G = - |z| F \int_o^x E \, dx \qquad (2.19)$$

where z = number of electrons involved in the redox reaction

F = Faraday constant

The measurement of the electrochemical curve therefore allows the calculation of the maximum energy which may be obtained from the cell.

At constant temperature, the Gibbs function $\Delta_r G$ of a reaction is related to the enthalpy and entropy terms by the equation:

$$\Delta_r G = \Delta_r H - T\Delta_r S \qquad (2.20)$$

with ΔG = Gibbs function [J]
ΔH = enthalpy [J]
ΔS = entropy [JK^{-1}]
T = temperature [K]

The enthalpy and entropy of a cell reaction can be calculated from the temperature coefficient of the cell, using the Gibbs - Helmholtz equation (eq. 2.21):

$$\left(\frac{\partial \Delta G}{\partial T}\right)_p = -\Delta S = \frac{\Delta G - \Delta H}{T} \qquad (2.21)$$

This equation can be expressed in terms of the Nernst potential by replacing ΔG with eq. 2.19:

$$-|z|\,F\left(\frac{\partial E}{\partial T}\right)_p = \frac{-|z|\,F\,E - \Delta H}{T} \qquad (2.22)$$

The entropy and enthalpy terms for the cell reaction are then given by the expressions:

$$\Delta S = |z|\,F\left(\frac{\partial E}{\partial T}\right)_p \qquad (2.23)$$

$$\Delta H = -|z|\,F\,E + |z|\,F\,T\left(\frac{\partial E}{\partial T}\right)_p \qquad (2.24)$$

The cell enthalpy and entropy terms can therefore be calculated by measuring the open-circuit voltage at different temperatures. It is stressed, however, that the reaction must be reversible, and must follow the same mechanism at all temperatures considered.

Lithium intercalation at ambient temperature frequently leads to metastable compounds, which transform to stable

compounds when heated. The reaction pathways are therefore often different at higher temperatures. A careful investigation of the reaction mechanism at different temperatures must therefore be undertaken before any calculation of ΔS and ΔH can be made. This is beyond the scope of this work, which deals mainly with the characterisation of ambient temperature reactions.

In the course of the discharge, the variations of the open-circuit voltage (i.e., the shape of the electrochemical curve) are indicative of the type of electrochemical process.

According to the Gibbs Phase Rule (eq. 2.25), the degrees of freedom of a system, f, are related to the number of components, c, and of phases, p:

$$f = c - p + 2 \qquad (2.25)$$

For a system at constant temperature and pressure, the Gibbs rule is reduced to the expression:

$$f = c - p \qquad (2.26)$$

Thus, in a ternary system $Li_xM_yO_z$, in which three components are required to define the phases of the system, at constant temperature and pressure, single-phase and two-phase regions will have f = 2 and f = 1 degrees of freedom respectively, allowing the equilibrium potential to vary.

In the case of a two-phase process, i.e., where two phases are formed from one initial phase, resulting in the presence of three different phases in the system, the number of degrees of freedom equals zero. In this case the cell voltage remains constant, resulting in a plateau when the o.c.v is plotted as a function of the electrode composition.

2.4 GALVANOSTATIC DISCHARGE CURVES

Although the electrochemical curve is useful to determine thermodynamic data, and to investigate the reaction mechanism, it does not entirely reflect the behaviour of a cell under load, i.e., the conditions in which a battery is used.

The galvanostatic (or constant current) discharge curve provides information on the operating voltage and efficiency of a cell, when discharged at a given current density.

A few concepts regarding the operating voltage and cell efficiency will be briefly mentioned in this section. The open-circuit voltage, measured at equilibrium, is a thermodynamic value, and can be calculated according to the Nernst equation (c.f. section 2.3). The value of the operating voltage of an electrochemical cell is lower: the voltage drop (or over-voltage, η) is due to polarisation.

Over-voltage is a function of the current density with which the cell is discharged, as expressed by the Tafel equation:

$$\eta = a - b \log I \qquad (2.27)$$

where η = over-voltage [V]
I = current density [A/cm^2]
a = constant for a specific electrode
b = constant given by

$$b = \frac{2.303\ RT}{\alpha F}$$

with R, T, F defined as in eq. 2.18
α = reciprocal of the number of electrons involved in the redox reaction (transfer coefficient)

There are three broad categories of polarisation effects:

a) activation polarisation, i.e., the energy necessary to initiate the electron transfer reaction

b) concentration polarisation, due to changes in the concentrations of the reactants in the electrodes and in the electrolyte. These changes counter diffusion, which would lead to a uniform concentration within the electrolyte and at the electrode - electrolyte interface

c) resistance polarisation, due to a number of factors, amongst which are:

- finite electronic conductivity of the electrodes
- finite ionic conductivity of the electrolyte
- changes of concentration of the electrochemically active species within the electrolyte (cf. point b)
- formation of solid products at the electrode surface.

In the case of intercalation electrodes, an over-voltage is also associated with the solid state diffusion of the intercalate in the host lattice [105,106].

A typical galvanostatic discharge curve is shown in Fig. 2.5. At the beginning of the cell discharge, the voltage drops at a uniform rate, which is a function of the current density (i.e., the discharge rate). Once the effects of polarisation for a particular system become constant, a voltage plateau is observed: this potential is termed the operating voltage of the cell. After a time t, the potential falls: beyond this point, often termed the "knee" of the curve, very little useful energy can be obtained from

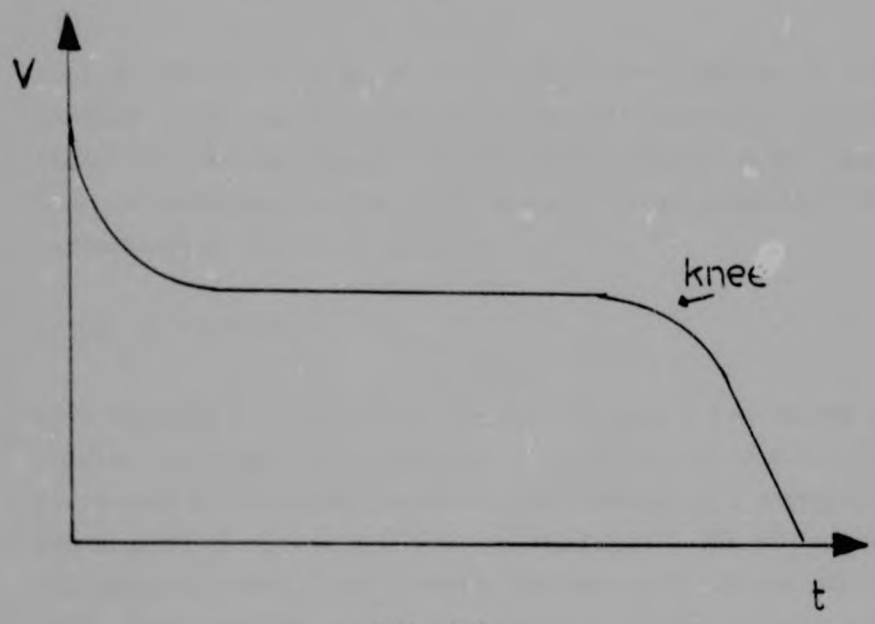


FIG. 2.5
Typical galvanostatic discharge curve

the system. The length of the voltage plateau depends on the discharge rate. An empirical relationship between current density and duration of discharge was first formulated by Peukert in 1897 [107]:

$$t\, I^n = k \tag{2.28}$$

where t = duration of discharge [min]
I = current density [A/cm^2]
n, k = constants ($n \approx 1.30 - 1.40$)

This expression is often given in the linear form:

$$n \log I = \log k - \log t \tag{2.29}$$

The constants n and k are characteristic of a particular system, and are usually determined empirically. It is generally accepted that the efficiency of an electrochemical

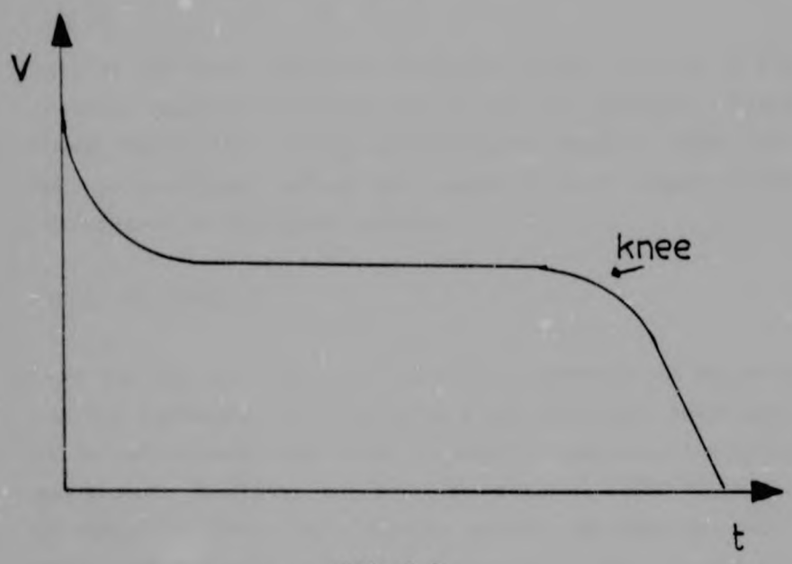


FIG. 2.5
Typical galvanostatic discharge curve

the system. The length of the voltage plateau depends on the discharge rate. An empirical relationship between current density and duration of discharge was first formulated by Peukert in 1897 [107]:

$$t\, I^n = k \tag{2.28}$$

where t = duration of discharge [min]
I = current density [A/cm^2]
n, k = constants ($n \approx 1.30 - 1.40$)

This expression is often given in the linear form:

$$n \log I = \log k - \log t \tag{2.29}$$

The constants n and k are characteristic of a particular system, and are usually determined empirically. It is generally accepted that the efficiency of an electrochemical

cell at different rates of discharge largely depends on the chemical reactions involved and on the cell geometry. Since these two factors cannot be separated easily, great care must be exercised during cell assembly when comparing the performance of different systems.

2.5 CYCLIC VOLTAMMETRY

Over the past 15 - 20 years, cyclic voltammetry has become a popular technique for examining electrochemical reactions. It is used increasingly today in electrochemistry, inorganic and organic chemistry and even biochemistry. The technique is useful to study such diverse aspects as reaction pathways, free radicals, enzymatic catalysis, ligand effects and solar energy conversion. Cyclic voltammetry has recently been applied to the study of intercalation electrodes [85, 90,96,108-111].

2.5.1 General principles

The principles of cyclic voltammetry will be briefly explained here.

In the cyclic voltammetry experiment a potential, applied between the working- and the counter-electrode, is varied linearly as a function of time, and the current resulting from a redox reaction is measured. A current - voltage curve (i.e., a voltammogram) is thus recorded.

The applied potential can be visualised as a triangular waveform (Fig. 2.6). The scan limits are termed "switching potentials": the scan direction is reversed when these values are reached.

A typical cyclic voltammogram for a single, reversible electrochemical process is shown in Fig. 2.7. The evolution of

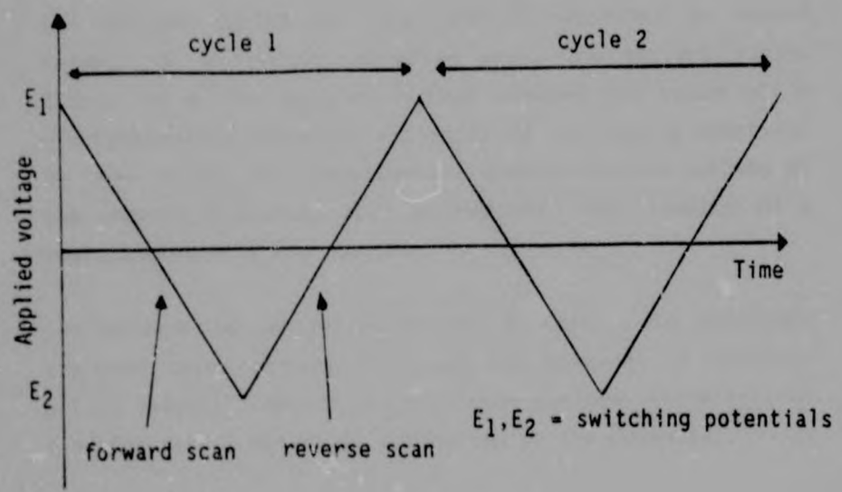


FIG. 2.6

Applied potential waveform in cyclic voltammetry

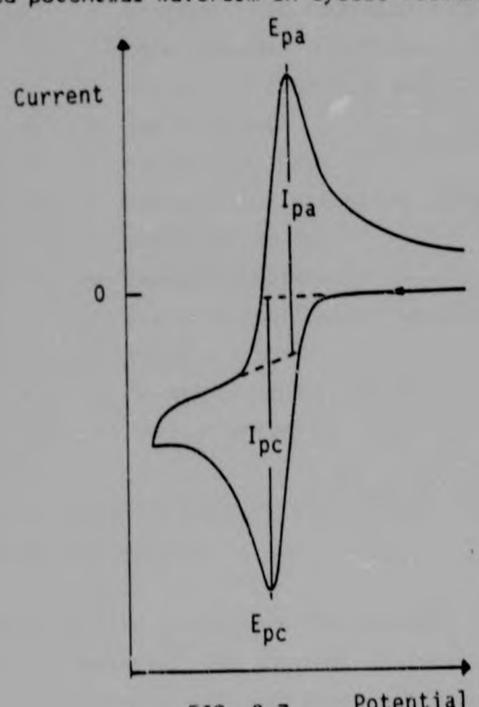


FIG. 2.7

Cyclic voltammogram of a single reversible process

the current during the scan can be described in simple terms. On a forward, negative scan, the current varies little until the applied voltage reaches the value of an electrochemical reduction potential of the system observed. At this value, the electroactive species at the surface of the working electrode will be reduced: this results in a rapid increase of the current.

The current is controlled by two factors: the electron-transfer rate constant (k_f) and the movement of electroactive material towards the electrode surface. The electron-transfer rate constant is a function of the potential:

$$k_f = k^0 \exp\left(\frac{-\alpha nF}{RT}(E - E^{0'})\right) \qquad (2.30)$$

where k^0 = standard heterogenous electron-transfer rate constant (particular to a reaction and to the electrode surface used)

R = gas constant

T = temperature [K]

n = number of electrons transferred per molecule [eq/mol]

F = Faraday constant

α = transfer coefficient (specific to a reaction, $0 < \alpha < 1$)

$E^{0'}$ = formal reduction potential [V]

E = applied potential [V]

The electron-transfer rate is responsible for the initial sharp rise of the current.

As the electroactive species in the vicinity of the working electrode is depleted, the process becomes diffusion-controlled. The cathodic current therefore peaks: reduction continues, but its rate depends on the diffusion of the electroactive species through the unstirred electrolyte.

The current will then be proportional to the slope of the profile describing concentration (C) versus distance from the electrode (x), according to the expression:

$$i = n F \alpha D_0 \left(\frac{\partial C_0}{\partial x}\right)_{x=0} = K \left(\frac{\partial C_0}{\partial x}\right)_{x=0} \qquad (2.31)$$

where i = current [A]
A = electrode area [cm^2]
D_0 = diffusion coefficient of the oxidised species [cm^2/s]
C_0 = concentration of the oxidised species [mol/cm^3]
x = distance from the electrode [cm]
n, F = as above.

The scan direction is then reversed. Diffusion-limited reduction continues until the electrochemical oxidation potential is reached. At this point, oxidation may occur: the reduced species, accumulated near the working electrode in the course of the forward scan, is oxidised, causing a rise of the anodic current. Once the reduced species close to the electrode is exhausted, the current decreases.

A series of equations describes the potentials and currents observed in the cyclic voltammetry experiment in the case of a fully reversible system.

The formal reduction potential for a reversible redox couple is generally given as $E^{0'}$:

$$E^{0'} = \frac{E_{pa} + E_{pc}}{2} \qquad (2.32)$$

with E_{pa} = potential at maximum current (anodic peak) [V]
E_{pc} = potential at maximum current (cathodic peak) [V].

This value represents a good estimate of the formal reduction potential, although it is not highly accurate. According to Nicholson and Shain [112], the average between E_{pa} and E_{pc} is really the polarographic half-wave potential $E_{1/2}$.

$E_{1/2}$ is a function of the oxidation and reduction diffusion coefficients (D_O and D_R):

$$E_{1/2} = E^{0'} - \frac{RT}{nF} \ln \{\frac{D_O}{D_R}\}^{1/2} \qquad (2.33)$$

The error introduced by the approximation $E_{1/2} = E^{0'}$, however, is small and usually neglected.

For a fully reversible electrochemical system, the separation between the anodic and the cathodic peaks depends on the number of electrons transferred, and is given by the equation:

$$\Delta E_p = E_{pa} - E_{pc} = \frac{0.059}{n} \qquad (2.34)$$

For an electrochemically reversible system, the anodic peak current equals the cathodic peak current:

$$i_{pa} = i_{pc} \qquad (2.35)$$

The peak current (i_p) is then given by the expression:

$$i_p = (2.69\ 10^5)\ n^{3/2}\ A\ D_O^{1/2}\ v^{1/2}\ C_O^* \qquad (2.36)$$

where i_p = peak current [A]
v = scan rate [V/h]
C_O^* = bulk concentration [mol/cm^3]
n, A, D as above

It must be stressed that equations 2.32, 2.34, 2.35 and 2.36 are only valid for fully reversible electrochemical systems.

An electrochemically reversible system is defined as a reaction that is sufficiently fast to maintain equilibrium between the oxidised and the reduced species at the electrode surface, according to the Nernst equation (eq. 2.18):

$$E = E^{0\prime} - \frac{RT}{nF} \ln \frac{[Ox]}{[Red]} = E^{0\prime} - \frac{0.059}{n} \log \frac{[Ox]}{[Red]}$$

Slow electron transfer or slow diffusion rates may result in "irreversibility": in this case an increase in the peak separation (ΔE_p) is observed, when the scan rate is increased.

Systems of this type are often termed "quasi-reversible" or simply "irreversible". When studying these reactions the scan rate should be adjusted in order to achieve "reversible" conditions.

When the distance between the cathodic and anodic peaks is such that they do not overlap at all, the system is generally called "totally irreversible". Amongst these systems are reactions that cannot be recycled at all, and often display no return peak during the reverse scan: these systems are "chemically irreversible".

In summary, cyclic voltammetry yields considerable information about an electrochemical system: reversibility, redox potentials, number of electrons involved (in the case of reversible systems), reaction kinetics, and fate of newly-formed species (in the course of irreversible processes).

2.5.2 Instrumentation

The instrumentation required for cyclic voltammetry comprises a waveform generator, a potentiostat, a current-to-voltage converter and an XY recorder.

The generator produces a triangular excitation signal which is transmitted to the electrochemical cell via the potentiostat. The potentiostat has the function of controlling the working-electrode potential during the reaction. The current-to-voltage converter measures the current. The voltammogram is finally displayed on an XY recorder, or on an oscilloscope in the case of very fast scan rates.

A three-electrode cell assembly is used for the cyclic voltammetry experiment: a working-electrode, a reference-electrode and a counter- or auxiliary-electrode.

A potential is applied between the working- and the counter-electrode; the latter also provides the current necessary at the working electrode. The voltage is measured between the working- and the reference-electrode, through which practically no current flows. The potential of the reference-electrode thus remains constant.

In order to minimise ohmic (iR) loss through the solution, the reference-electrode is placed very close to the working-electrode. For this purpose, a Luggin capillary is sometimes used.

2.5.3 Cyclic voltammetry of intercalation systems

This technique is becoming increasingly widespread in the field of intercalation chemistry, since it provides a rapid initial evaluation of potential electrode materials, and helps to describe the reaction mechanism [85,86,90,96,108-111,113-115].

A conventional three-electrode assembly is used. Lithium metal (generally in the form of foil or wire) is employed for both the counter- and the reference-electrode. The working-electrode, e.g., a transition metal oxide or sulphide, is usually a powder, compacted or deposited onto a current collector (a piece of metal gauze or foil). Very small quantities (a few mg) of powder are used, pressed to form a thin film. Conventional electrolytes for lithium intercalation systems, i.e., lithium salts dissolved in aprotic organic solvents, are used in cyclic voltammetry cells. Because cyclic voltammetry experiments are of relatively short duration, when compared to charge/discharge cycling tests, mixtures of organic solvents are often chosen with an emphasis on high conductivity rather than long-term lithium-solvent stability.

Full electrochemical reversibility, as defined in eq. 2.34 is seldom observed in intercalation systems; quasi-reversible conditions can be attained by using very slow scan rates, typically in the order of 0.1 - 1 mV/sec or slower.

It is generally accepted [116-118] that the rate-determining factor in lithium intercalation cells is the diffusion of lithium ions within the lattice. This process is much slower than both the electron-transfer rate and the transport of lithium cations in the electrolyte.

A study of the cyclic voltammograms as a function of the scan rate therefore gives good indications on the lithium diffusion coefficients in the material under investigation.

A qualitative analysis of the cyclic voltammograms of intercalation processes yields the following information:

- number of processes involved
- oxidation/reduction potentials of each process

- reversibility of each reaction
- fate of the reacted species (appearance of new processes, reversibility, etc.)
- qualitative assessment of the diffusion rates by variation of the scan rates
- relative diffusion rates (comparison of different processes within the same system).

This information, in turn, leads to an initial assessment of the cell operating voltage, the number of discharge plateaux and the reaction mechanism(s).

Quantitative interpretations of the cyclic voltammetry of intercalation systems have recently been proposed [86,113, 114]. Models have been developed for the determination of phase diagrams [113], the differential capacity of intercalation electrodes [86], and lithium diffusion coefficients [114]. The success of most of these methods requires a very meticulous preparation of a thin film electrode and extremely slow scan rates. Other methods are therefore often preferred for quantitative investigations.

In this work, only qualitative interpretations will be given, due to the lack of very slow scan rates on the available equipment.

2.6 LITHIUM DIFFUSION RATES ($\tilde{D}$)

2.6.1 General principles

The current-voltage curves discussed in Section 2.4 are important for the determination of the power density of a battery system. As I-V curves can be recorded easily, they are

Author De Picciotto L A
Name of thesis Topochemical reactions of Lithium with transition metal oxides 1988

PUBLISHER:
University of the Witwatersrand, Johannesburg
©2013

LEGAL NOTICES:

Copyright Notice: All materials on the University of the Witwatersrand, Johannesburg Library website are protected by South African copyright law and may not be distributed, transmitted, displayed, or otherwise published in any format, without the prior written permission of the copyright owner.

Disclaimer and Terms of Use: Provided that you maintain all copyright and other notices contained therein, you may download material (one machine readable copy and one print copy per page) for your personal and/or educational non-commercial use only.

The University of the Witwatersrand, Johannesburg, is not responsible for any errors or omissions and excludes any and all liability for any errors in or omissions from the information on the Library website.